Tungsten (2023) 5:440–466
https://doi.org/10.1007/s42864-022-00174-1

Tungsten
www.springer.com/42864

REVIEW PAPER

A review of the effect of tungsten alloying on the microstructure and properties of steels

Jun-Jie Lian[1,2,3] · Xiao-Guang Ma[1,2,3] · Zheng-Yi Jiang[4,5] · Chong Soo Lee[6] · Jing-Wei Zhao[1,2,3]

Received: 31 May 2022 / Revised: 26 July 2022 / Accepted: 27 August 2022 / Published online: 22 September 2022

Abstract

With the continuous development of science and technology, the increasingly severe service environment makes people put forward higher requirements for the performance of alloy steel. Tungsten has unique properties such as excellent strength, high density and good hardness, and its addition as an alloying element will change the properties of alloy steel. This paper aims to summarize the effect of the addition of tungsten on the microstructure and mechanical properties of alloy steel. The background of research and application of tungsten alloyed steel is presented initially. Then, the preparation methods of tungsten alloyed steel are described. Next, the effect of tungsten incorporation on the microstructure of alloy steel is reviewed. Finally, the effects of tungsten addition on the mechanical properties, corrosion resistance and hydrogen embrittlement resistance of the alloy steel are reviewed. This review provides an outlook on the development of tungsten alloyed steel, which will stimulate more in-depth research and ultimately promote the practical application of tungsten alloyed steel.

Keywords Tungsten · Alloy steel · Microstructure · Properties

1 Introduction

With the continuous development of science and technology, the performance requirements of materials under different environmental conditions are becoming increasingly critical. Tungsten (W) is a metallic element with ultra-high strength, density and melting point. Therefore, these properties create attractive prospects for the application of W in extreme engineering environments. However, W is a rare metal and is highly brittle, making it difficult to directly apply in industrial production. Thus, many studies have combined W with other metal elements to form composite materials. For example, W–Cu composites with high electrical conductivity, high thermal conductivity and high hardness [1, 2], Al–W alloys with corrosion resistance and oxidation resistance [3], etc. This study mainly reviews the effects of W in steel. The addition of W can optimize the microstructure of the steel and improve the mechanical properties and corrosion resistance of steel. The application of tungsten alloying in steel is reviewed as follows [4]:

1. High-speed steels. High-speed steels are a kind of special steel with excellent performance. They have a high working hardness, wear resistance, heat resistance and excellent toughness at temperatures up to 500 °C attributed to the presence of W, Mo, Al and other alloying elements. Therefore, they are mainly used to manufacture complex thin-edged and impact-resistant metal cutting tools, as well as high-temperature bearings and cold extrusion dies.

✉ Jing-Wei Zhao
jzhao@tyut.edu.cn

1 College of Mechanical and Vehicle Engineering, Taiyuan University of Technology, Taiyuan 030024, China

2 Engineering Research Center of Advanced Metal Composites Forming Technology and Equipment, Ministry of Education, Taiyuan 030024, China

3 Taiyuan University of Technology-University of Wollongong (TYUT-UOW) Joint Research Center, Taiyuan University of Technology, Taiyuan 030024, China

4 School of Mechanical, Materials, Biomedical and Mechatronic Engineering, University of Wollongong, Wollongong, NSW 2522, Australia

5 TYUT-UOW Joint Research Center, University of Wollongong, Wollongong, NSW 2522, Australia

6 Graduate Institute of Ferrous and Energy Materials Technology, Pohang University of Science and Technology, Pohang 37673, South Korea

2. Tool steels. Tool steels are the steels used to manufacture cutting tools, measuring tools, molds and wear-resistant tools. According to different chemical compositions, tool steels are generally classified as carbon tool steels, alloy tool steels and high-speed tool steels. Tool steels contain a large number of alloying elements including W, Mo, V, Cr, Mn and Co. Alloying elements such as W, Mo, V and Cr are strong carbide formers, which provide high hardness, excellent wear resistance and good size control during the application heat treatment of tool steels [5].
3. Heat-resistant steels. Heat resistant steels are alloy steels with high strength and good chemical stability at high temperatures. The most important alloying elements in heat-resistant steels are chromium for oxidation and nickel for strength and ductility. Other alloying elements, including Mn, Mo, W, Ti, V, Nb, Al, Co, Cu, B and rare earth elements such as Ce, La and Y, are usually added in different combinations to improve the comprehensive high-temperature properties of steels. The addition of appropriate amounts of W to heat-resistant steels is beneficial in improving the high-temperature tensile strength, fracture toughness, creep fatigue resistance and long-term service stability [6, 7]. Heat-resistant steels are often used in the manufacture of boilers, steam turbines, power machinery and industrial furnaces, as well as the parts working at high temperatures in aviation, petrochemical and other industrial sectors [8].
4. Stainless steel (SS). SSs are a kind of special alloy steel used primarily for corrosion resistance. Other desirable properties may include excellent formability, good resistance to oxidation and creep at elevated temperatures. Chromium alloying element must be at least 12 wt.% by weight to provide the corrosion resistance of SS, while many other alloying elements, including Ni, Mo, W, Mn, Si and Cu, can be added to stabilize other phases to provide additional resistance and/or produce enhanced mechanical properties. Attributed to the interaction between W and positive ions and the inhibition of tungstate, W plays a beneficial role in improving the passivation performance of SS, thereby improving its corrosion resistance [9].
5. Other steels. In addition to the steels mentioned above, W is also used in structural steels for fusion reactors [10], valve steels for automobile engines [11], heat-resistant and wear-resistant steels for burner nozzles, sag resistant steels for springs [12], maraging steels for engine components [13, 14] and high Co–Ni steels for aircraft [15].

With the development of industry, the demand for tungsten alloyed steel is increasing. This review introduces the preparation methods of tungsten alloyed steel, the influence of tungsten on the microstructure of steels, the effect of tungsten on the mechanical properties of steels and the effect of tungsten on the corrosion resistance and hydrogen embrittlement (HE) resistance of steels. This review brings these together to provide a succinct resource from which scholars developing new materials or requiring strategies to process troublesome materials may find inspiration.

2 Preparation methods of tungsten alloyed steel

Tungsten alloyed steels are a type of alloy made of tungsten (tungsten carbide) mixed with steel [16–18]. As early as the 1750s, chemists discovered the effect of tungsten on the properties of steel. By 1859, Wurm [19] discovered that when the addition of W was 2 wt.%–5 wt.%, the hardness of steel could be greatly increased without damaging its toughness and ductility. At the end of the nineteenth century and the beginning of the twentieth century, tungsten alloyed steel began to be produced and widely used. In 1868, Mushet invented self-hardening steel composed of 2.5% Mn-7% W (wt.%), which improved the cutting speed to 5 $m \cdot min^{-1}$ [20]. In 1898, Taylor, an American mechanical and management engineer, and White, a metallurgist, developed high-speed steel and made a systematic cutting test [21]. The emergence of this kind of steel also marks major technological progress in the field of metal cutting and processing. This section mainly introduces the preparation methods of tungsten alloyed steel and the advantages and disadvantages of each preparation method.

2.1 Sand casting

Tungsten alloyed steel can be prepared using sand casting in which the casting is produced in a sand mold. Sand casting involves pouring molten metal into a mold cavity made of sand to make relatively large parts. It has been used to make metal products since the Shang Dynasty in China more than 3000 years ago [22]. At present, sand casting is an important manufacturing process in the oil and gas, aerospace and automobile industries [23]. Steel, iron and most non-ferrous alloy castings can be obtained by sand casting methods. Traditional sand casting is shown in Fig. 1 [22]. The molding materials used in sand casting are cheap and easy to obtain, and mold manufacturing is simple. Sand casting is suitable for single-piece production, batch production and mass production of castings. Sand casting has been the basic process in casting production for a long time. The type and content of alloying elements can be controlled in castings. However, the quality of molding sand and core sand directly affects the quality of the casting. Defects such as pores, blisters, sand

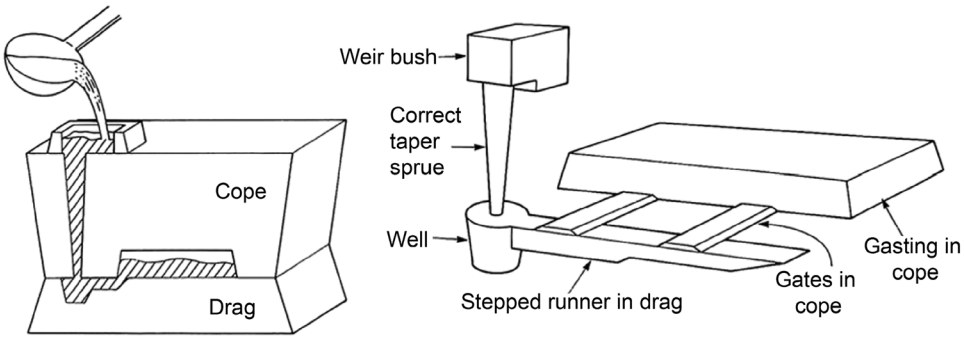

Fig. 1 Structure of sand molding and typical gating system. Reproduced with the permission from Ref. [22]. Copyright 2022 Elsevier

sticking and sand inclusions of the casting may be caused due to the poor quality of the molding sand.

Sand casting facilitates the production of castings with high quality. However, with the acceleration of the replacement of parts, while the parts are eliminated, the molds are also affected, which results in a serious waste of resources. To solve these problems, rapid casting has been developed. This technology is the integration of three-dimension (3D) printing and traditional casting [24]. In this technology, a disposable pattern for forming a mold is created using 3D printing technology, which shortens the product design time and increases the advantages of the foundry industry [25].

2.2 Vacuum induction melting

Vacuum induction melting (VIM) was developed in the early 1950s, stimulated by the need to produce superalloys containing reactive elements within an evacuated atmosphere. It is suitable to be used to prepare tungsten alloyed steel [26]. VIM is a melting process in which eddy current is generated in the metal conductor by electromagnetic induction under vacuum conditions. The typical VIM device is shown in Fig. 2a [27]. The melting process of VIM includes selecting and preparing crucible, charge preparation, melting, refining and pouring. Compared with conventional melting, VIM has the following advantages:

1. Low oxidation loss of alloy elements;
2. Precise temperature control;
3. Low level of environmental pollution from dust;
4. Remove undesired trace elements with high vapor pressure;
5. Remove dissolved gases such as hydrogen and nitrogen.

The toughness [28, 29], fatigue strength [28], corrosion resistance [30], creep strength [31–33] and permeability of magnetic alloy and other properties [12, 34, 35] can be improved by VIM. However, the disadvantage of VIM is that most final products require remelting, mainly to reduce segregation and control the solidification structure and erosion of refractories.

2.3 Vacuum arc melting

Vacuum arc melting (VAM) is an electrothermal metallurgical method of smelting metals by using electric energy to generate an electric arc between electrode and electrode or between electrode and materials to be smelted. Currently, it is commonly used to research and manufacture refractory metals and metal carbides in the laboratory. Tungsten is one of the most refractory metal elements, some studies have used VAM to prepare tungsten alloyed steel with excellent properties [36–38].

Figure 2b is a schematic diagram of VAM with a consumable electrode [39]. The quality of the resulting alloy depends on the cooling rate and the gap between the electrodes and the current [40, 41]. Processing parameter control is important, which can be directly related to the uniformity and properties of materials [39]. Different from the traditional metallurgical process, it can accurately control the composition of alloying elements. The products made by VAM have few impurities, low gas content, good ingot structure, excellent mechanical and physical properties. Indian reduced activation ferritic-martensitic steels [42] are obtained by VIM followed by VAM. Through VAM, the elements that promote embrittlement, such as S, P, As, Sb, Sn, Zr and O, are limited to the parts per million level, which ensures uniform structure and no segregation of the ingot. VAM has been widely used in aerospace, nuclear power and military industries [42–45].

2.4 Hot isostatic pressing

Hot isostatic pressing (HIP) is a production technology integrating high temperature and high pressure. High-performance tungsten alloyed steel can be prepared by the HIP. The configuration of the standard HIP unit is shown in Fig. 2c [46]. The heating temperature of the HIP is usually 1000–2000 °C, and the working pressure can reach 200 MPa by using high-pressure inert gas or nitrogen as a pressure transmission medium in a closed container. Under the combined action of high temperature and high pressure, the workpiece is uniformly compressed in all directions.

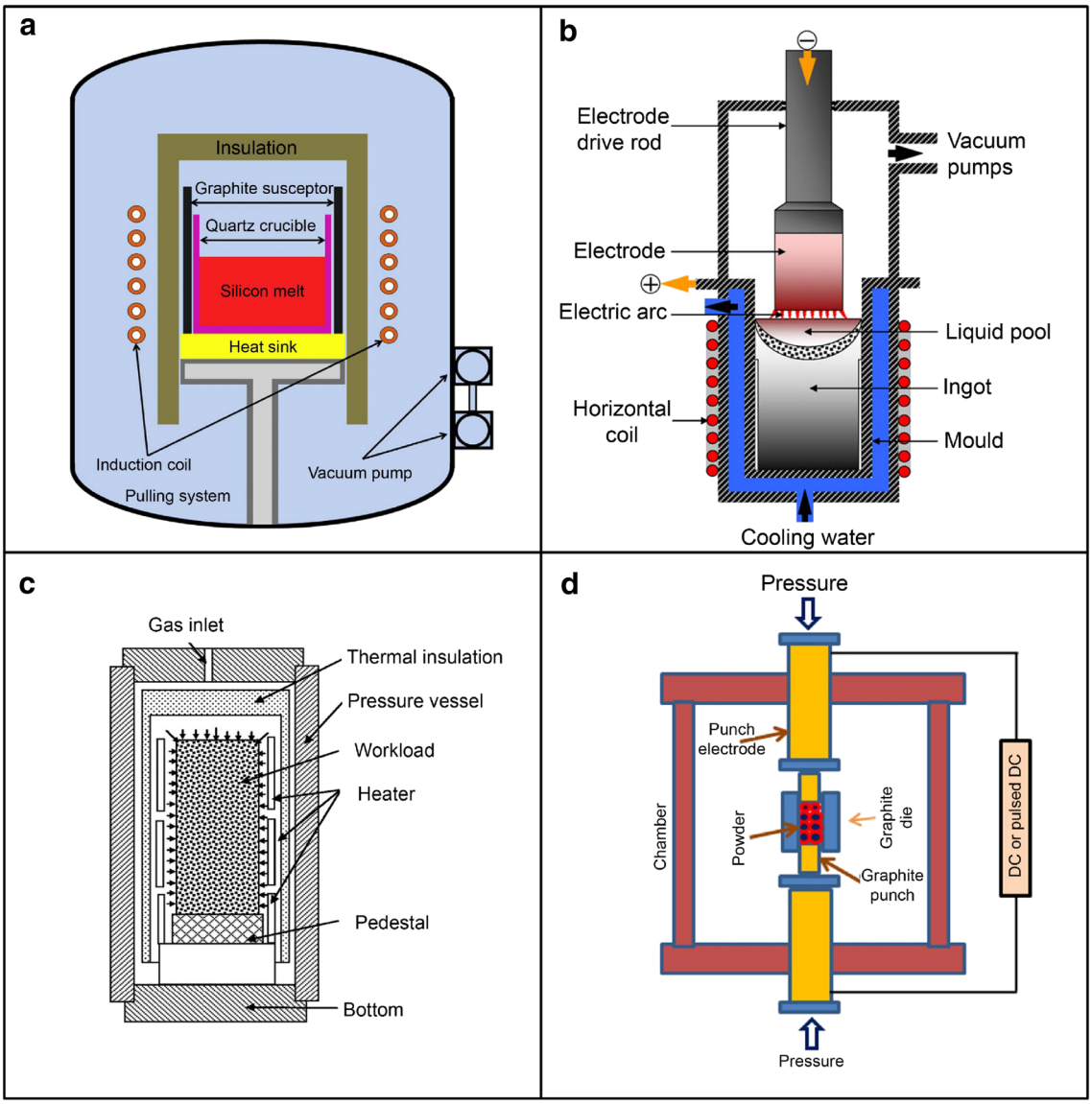

Fig. 2 Schematic diagram of the **a** VIM. Reproduced with the permission from Ref. [27]. Copyright 2014 Elsevier. **b** VAM. Reproduced with the permission from Ref. [39]. Copyright 2010 Elsevier. **c** HIP. Reproduced with the permission from Ref. [46]. Copyright 2013 Elsevier. **d** SPS. Reproduced with the permission from Ref. [56]. Copyright 2018 Elsevier

Therefore, the processed products have high compactness, good uniformity and excellent performance. The HIP is suitable for parts in the approximate weight range of 20 kg–15 tons [47].

HIP can be used to produce products with uniform microstructure and fine grains at a lower sintering temperature. At the same time, HIP has the characteristics of a short production cycle, few procedures, low energy consumption, low material loss and high cleanliness of steel [47]. Composites with excellent properties can be obtained by controlling the ratio of various elements in the mixed powder [48–50]. However, the complexity of the HIP packaging process, the high one-time investment and the operating costs of the equipment have hindered the widespread use of the process in the industry.

2.5 Spark plasma sintering

Spark plasma sintering (SPS) is a highly efficient powder metallurgical process widely used for sintering ceramics and metallic materials [51, 52]. It can also be used to prepare tungsten alloyed steel. SPS is a pressure-assisted pulsed electric current sintering process utilizing ON–OFF direct current (DC) pulse energizing [53, 54]. With repeated application of ON–OFF DC pulse current in the powder material, the spark discharge point and the Joule heating point (local

high-temperature state) are transferred and dispersed over the entire specimen [55]. A simplified schematic is reproduced in Fig. 2d [56]. SPS effectively uses the internal heat of the powder to carry out sintering. The advantages of SPS are as follows:

1. Fast heating speed, low sintering temperatures, uniform heating, short sintering time and high production efficiency [57],
2. High-density material can be obtained [58],
3. Sinter gradient materials and complex workpieces [59, 60].

SPS has been widely used to prepare nanostructured materials [61, 62], functional gradient materials [63], cemented carbide [64], titanium alloys [65], bioceramics [66], porous materials [67], diamond, etc. [68]. The promotion of SPS will play an important role in the field of research and the production of new materials. However, the underlying theory of SPS is not fully understood yet, and a lot of practical and theoretical research is needed to improve it. In the future, it is necessary to develop fully automated SPS production systems to meet the production needs of complex shapes, high-performance products and three-dimensional gradient functional materials.

2.6 Microwave sintering

Microwave sintering is a technique for high-temperature material processing. Microwave sintering can be used to prepare ceramic materials or metallic materials, including tungsten alloyed steel [69]. Microwave sintering generates heat through the interaction between the special band of microwave and material particles, and densification is realized by heating the whole stuff to the sintering temperature through the dielectric loss of the material. This is different from the traditional method, which transfers heat between objects through mechanisms such as conduction, radiation and convection. However, microwave heating first generates heat inside the material and then heats the entire volume [70]. Microwave sintering is generally faster, cleaner and more economical than conventional methods [71]. A schematic of a typical microwave system, which is typically used to process metallic materials, is shown in Fig. 3 [72]. The microwave system is capable of operating in control atmosphere and temperatures up to 1600 °C [73].

However, the dielectric loss characteristics of various materials vary with frequency, temperature and impurity content and a database related to this needs to be established. As microwave sintering furnace is highly selective for the product, different products require microwave oven parameters to vary greatly. Therefore, microwave sintering furnace equipment requires a huge investment. The future direction of microwave sintering equipment is to integrate with modular design and computer control.

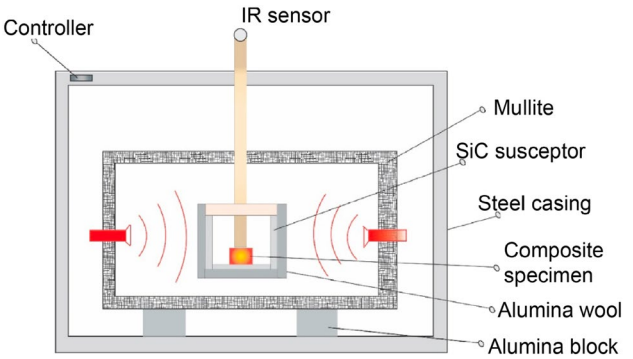

Fig. 3 Schematic of a multimode microwave processing system for metallic materials. Reproduced with the permission from Ref. [72]. Copyright 2022 Elsevier

2.7 Additive manufacturing

Additive manufacturing (AM) is a technique for layered forming of materials using a laser or electron beam as the heat source in combination with computer-aided design/computer-aided manufacturing (CAD/CAM) [74]. AM is used to prepare tungsten, tungsten-based alloys and tungsten-based composites because of its excellent design flexibility [75–78]. AM methods such as wire-arc additive manufacturing, electron beam melting, laser powder bed fusion and laser direct energy deposition are often used to prepare tungsten alloyed steel [79–82]. The diagram of the laser powder bed fusion is shown in Fig. 4 [83]. A high-energy laser beam completely melts a pre-covered metal powder following a predetermined scanning path, and then the molten powder is cooled and solidified to form the designed shape. AM has the following characteristics:

1. The molding raw material is generally a metal powder, mainly including SS, nickel-based high-temperature alloys, titanium alloys, cobalt-chromium alloys, high-strength aluminum alloys and precious metals.
2. The parts prepared by AM are highly accurate. The surface can meet the requirements of accuracy in use after simple post-treatment such as grinding and sandblasting.
3. The formed parts prepared by AM have good mechanical properties and can be used to prepare complex surfaces and structures in the aerospace field [84].

However, AM is currently not suitable for manufacturing large monolithic parts. Due to the high cost, AM is only used in a few industries such as medical, automotive and aerospace. Despite the great potential of AM, there are still some issues that need to be addressed, such as

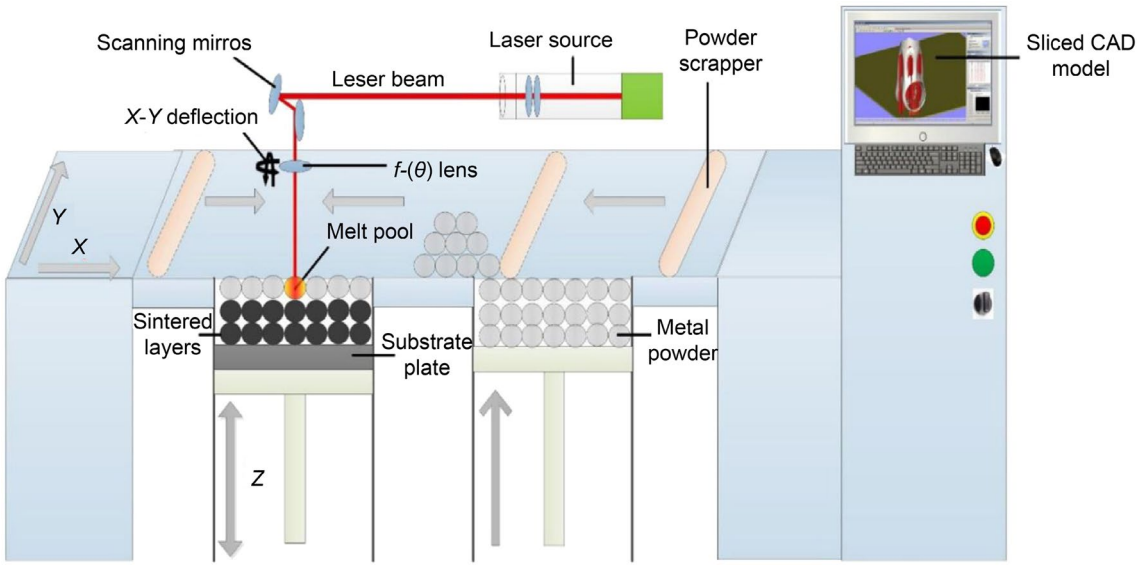

Fig. 4 Schematic illustration of selective laser melting process. Reproduced with the permission from Ref. [83]. Copyright 2020 Elsevier

material incompatibility and material cost. Future research could develop and modify the process to accommodate a wide range of materials.

In addition to the methods described, there are also some other preparation methods [85–89]. It can be expected that future preparation methods will be developed toward higher adjustable temperature, faster heating rate, controlled cooling rate and precise control of elemental content.

3 Effect of tungsten on the microstructure of steels

The properties of tungsten alloyed steel are determined by the chemical compositions and microstructure. To better understand the relationship between microstructure and properties, it is necessary to have a basic understanding of the solid phase transformation that occurs in tungsten alloyed steel. In this section, the effect of W on the continuous cooling transition (CCT) of microalloyed steels is first presented and the effect of W addition on the microstructure of microalloyed steels is discussed. With the increase of W content, it is necessary to regulate the phase composition of alloy steel by the Fe–W equilibrium phase diagram. The development of Fe–W binary phase diagrams is reviewed. The desired microstructure can be obtained according to the Fe–W binary phase diagram. Finally, taking the common Fe–W–C system and Fe–W–Cr system as examples, the development of W in the ternary alloy system and its influence on phase are introduced.

3.1 Effect of tungsten on microstructural evolution

The addition of micro-alloyed elements such as Nb, V, W and Ti in low carbon steel can significantly improve its mechanical properties. This kind of steel is called "microalloyed steel". It is well known that pearlite, pre-eutectoid, bainite, martensite and various ferritic microstructures are all based on austenite as the parent phase. At different chemical compositions and cooling rates, the austenite of microalloyed steel can be transformed into all of the microstructures listed. In microalloyed steel, the W content largely determines the microstructure and mechanical properties [90, 91]. Therefore, interest has been attracted regarding the effect of different W contents on the microstructure of microalloyed steel. The CCT diagrams play an invaluable role in characterizing the phase transformation properties of non-isothermal heat-treated steels and in revealing the influence of alloying elements on the steel organization.

The CCT diagram is obtained by varying the cooling rate from 0.1 to 120 °C·s^{-1}, as shown in Fig. 5 [92]. And F is ferrite, P is pearlite, B is bainite, M is martensite, M_s is the starting temperature of martensitic transformation, and M_f is the end temperature of martensitic transformation ions. Three different microalloyed steels with W content of 0, 0.1 and 1 wt.% are noted as 0 W, 0.1 W and 1 W, respectively. With the increase of W content, the range of transformed ion products shifts to the right of the diagram. When the cooling rate is 0.1–1 °C·s^{-1}, the CCT diagram of steel with 1 wt.% W is similar to that of steel without W. With the addition of W, both the start temperature and end temperature of austenitization increase. At the same time, the addition of W reduces the critical cooling rate of the phase transformation,

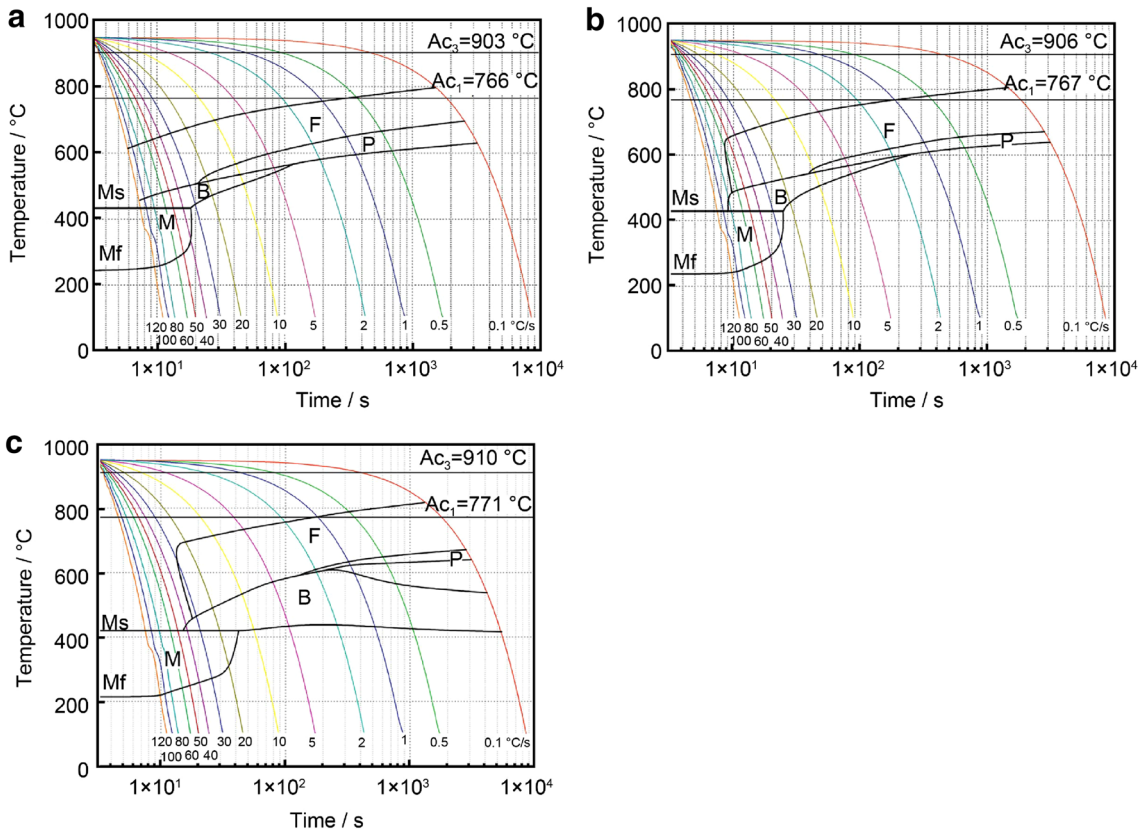

Fig. 5 CCT diagram of W-containing steels, **a** 0 W steel, **b** 0.1 W, **c** 1 W. Reproduced with the permission from Ref. [92]. Copyright 2013 Elsevier

and the complete ferrite + pearlite structure is obtained. Furthermore, the addition of W decreases the martensite transition temperature.

The composition of microalloyed steel is shown in Table 1. The microstructures of 0 W, 0.1 W and 1 W steels with continuous cooling are shown in Fig. 6 [92]. The label in the upper right corner of each figure represents the cooling rate. At the cooling rate of 0.5 °C·s^{-1}, the microstructure of 0 W and 0.1 W steels consist of ferrite and pearlite (Fig. 6a, d), while the microstructure of 1 W steel presents bainite in addition to ferrite and pearlite (Fig. 6g). When the cooling rate is increased to 30 °C·s^{-1}, the microstructure of 0 W steel is a mixture of ferrite and bainite (Fig. 6b), and 0.1 W steel shows a mixture of ferrite, bainite and martensite (Fig. 6e). When the content of W raises to 1 wt.%, the microstructure of microalloyed steel comprises mainly martensite with a small amount of ferrite and bainite (Fig. 6h). When the cooling rate reaches 120 °C·s^{-1}, the microstructure of 0 W steel composes of martensite, bainite and a small amount of ferrite, with martensite predominating (Fig. 6c). When the content of W increases to 1 wt.%, the microstructure is all transformed to martensite (Fig. 6i). Therefore, it can be seen that the addition of W has a significant effect on the microstructure of microalloyed steel. The best combination of strength and plasticity can be obtained by controlling the cooling rate to adjust the microstructure composition of microalloyed steel [91].

Table 1 Chemical compositions of steels with different W contents (wt.%) [92]

Specimens (W)	C	Mn	Cr	Ni	Cu	Si	Al	V	Nb	Ti	P	S	N	W
0	0.17	1.2	0.1	0.02	0.02	0.47	0.02	0.01	0.02	0.02	0.01	0.01	0.006	0
0.5	0.17	1.2	0.1	0.02	0.02	0.47	0.02	0.01	0.02	0.02	0.01	0.01	0.006	0.1
1	0.17	1.2	0.1	0.02	0.02	0.47	0.02	0.01	0.02	0.02	0.01	0.01	0.006	1

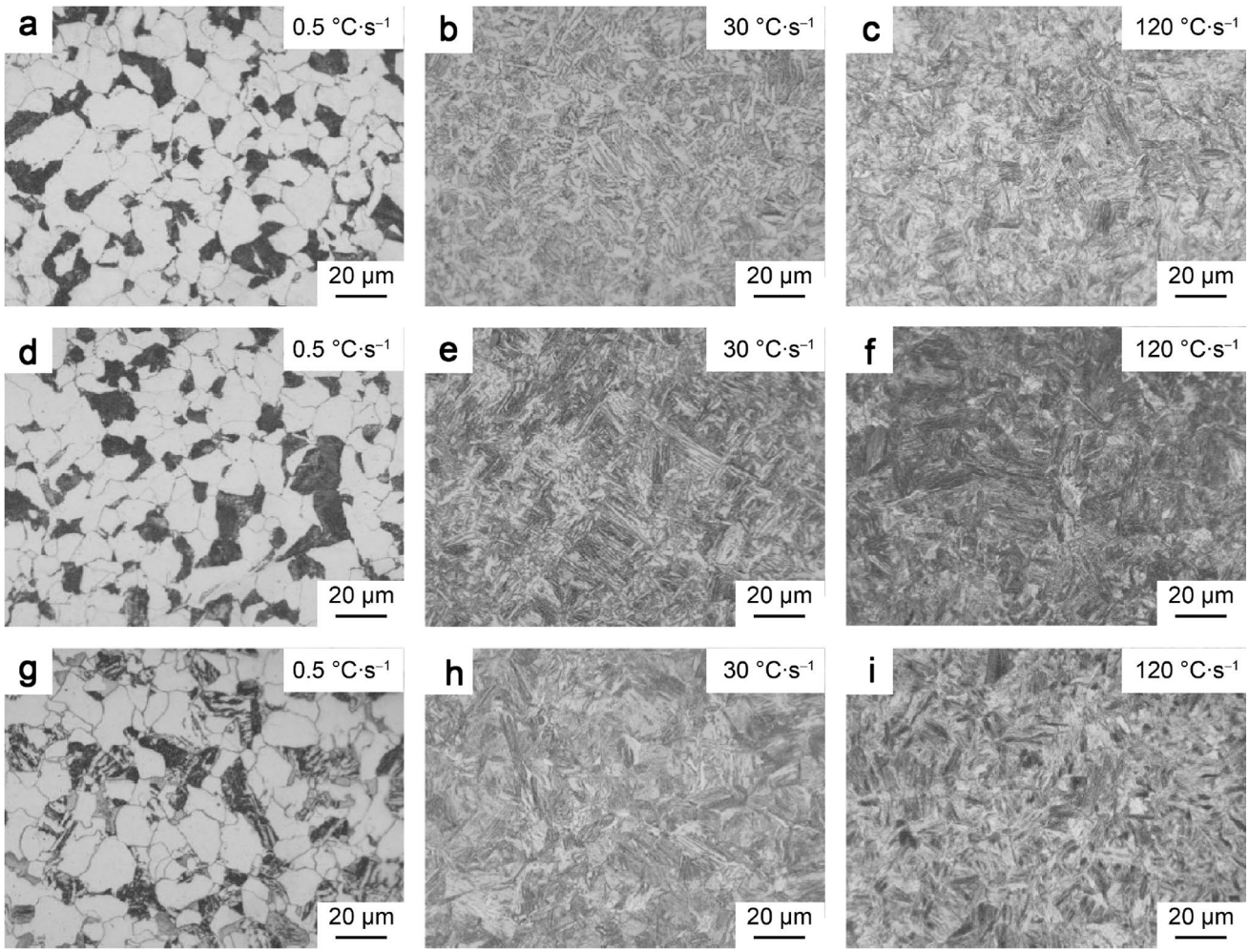

Fig. 6 Microstructures of continuously-cooled specimens. **a–c** 0 W, **d–f** 0.1 W, **g–i** 1 W. Reproduced with the permission from Ref. [92]. Copyright 2013 Elsevier

3.2 Fe–W binary phase diagram

Fe–W system constitutes the basis of industrial tungsten ferroalloy. The system applies to the research of steel, especially the further development of Fe_2W reinforced ferritic steel [93–95]. There are several experimental and theoretical reports on the Fe–W system. The consensus is the condensed phases in the Fe–W system are the liquid phase, terminal solid solution (W), body center cubic-Fe (BCC-Fe) and face center cubic-Fe (FCC-Fe) forming a closed loop, λ-Fe_2W and μ-Fe_7W_6 [96]. However, some early studies indicated the existence of the FeW phase in the Fe–W system. This controversy is mainly due to the slow reaction kinetics of FeW's formation, and it is difficult to determine its stability and instability through experiments [97]. Henig et al. [98] believed that the new phase FeW is formed by Fe_7W_6 and W-rich solid solution. With the in-depth study of the Fe–W system, many studies show that the FeW phase is not found in the Fe–W system [99, 100]. Zdziobek et al. [99] suggest that the previously reported phase FeW is likely to be ternary carbides with low carbon content. Therefore, it is generally believed that the FeW phase does not exist in the Fe–W binary system at present.

The Fe–W binary system itself has been thoroughly studied. It is characterized by a closed iron ring between 912 and 1394 °C. At present, several versions of experimental diagrams are proposed. The main arguments are about the extension of the Fe_7W_6 phase and Fe_2W phase. In addition to these intermetallic phases, a gamma ring appears that separates the austenitic γ-Fe phase from the ferrite α-Fe phase. Based on the Calphad method, Jacob et al. [96] established thermodynamic data sets for binary Fe–W systems. by using the PARROT module of Thermo-Calc software. As shown in Fig. 7 [96], their study utilized both experimental data from the available literature and thermodynamic data of intermetallic intermediate phases based on atomic computational

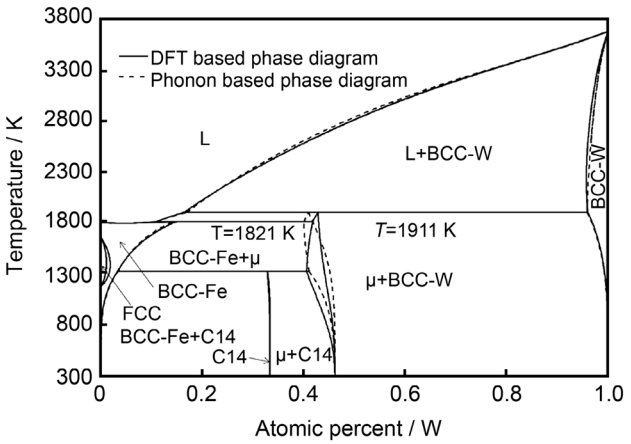

Fig. 7 Comparison of the two optimized phase diagram, in gray the calculated phase diagram from DFT and in black the calculated phase diagram using phonon. Reproduced with the permission from Ref. [96]. Copyright 2015 Elsevier

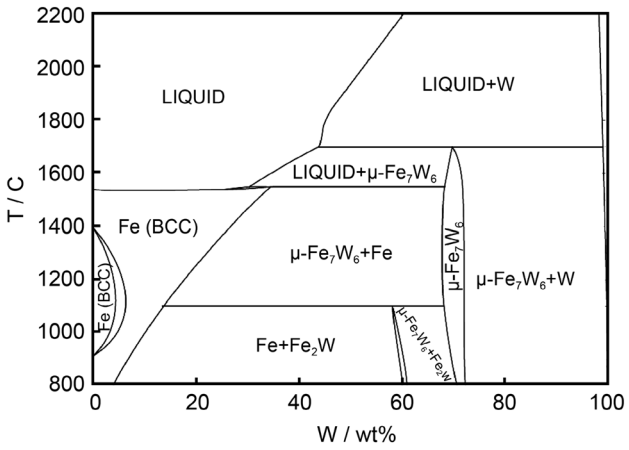

Fig. 8 Fe–W phase diagram II. Reproduced with the permission from Ref. [105]. Copyright 2013 Elsevier

tools. According to the chosen sublattice models, two different phase diagrams of the system are drawn by using the enthalpy of formation data at 0 K from density functional theory (DFT) and the finite temperature Gibbs energies calculated by phonons, respectively. At the same time, the authors point out that for partially disordered phases, they should be used with caution.

Okamoto [97] reviewed the previous literature on Fe–W and adopted one of the two Fe–W phase diagrams calculated by Jacob [96]. As shown by the solid line in Fig. 7 [96], it is very consistent with the data reported in many previous works of literature [99–104]. In particular, the characteristics of the Fe-rich side have attracted considerable attention, while the characteristics of the W-rich side are less obvious. Gasik [105] also gave the Fe–W alloy phase diagram, as shown in Fig. 8. The difference is that on the W-rich side, the boundary between Fe_2W and Fe_7W_6 is different from that of Jacob [96]. Regarding this controversy, at present, we have not found suitable literature to explain it. In addition, more research is needed to explain this controversy.

3.3 Effect of tungsten on ternary phase diagrams

According to the phase diagram of Fe–W binary alloy, the designed phases can be obtained. However, the metal materials used in industry, such as various alloy steels and non-ferrous alloys, are mostly composed of more than two kinds of components. The microstructure, properties, corresponding processing and treatment processes of these materials are usually different from binary alloys because the solubility between the components of the original alloy will be changed and even a new phase transformation will occur after adding the third component to the binary alloy. The developments of W in ternary alloy systems and their effects on phases are presented as examples of the common Fe–W–C system and Fe–W–Cr system.

Uhrenius [106] inferred the isothermal cross sections of the Fe–W–C system at higher temperatures by using the phase diagram information and thermochemical data of binary Fe–C, Fe–W and W–C systems in combination with the equilibrium information of the Fe–W–C system at 1000 °C. The main phases are α phase, γ phase, liquid phase, WC, μ-Fe_3W_2 and M_6C. Gustafson [107] evaluated the Fe–W–C system using a magnetic two-sublattice subregular model for the interstitial solution phases, a multiple lattice model for intermetallic phases and ternary carbides, and an ordinary sublattice solution model for the liquid phase, and gave a set of parameters describing the Gibbs energy of each phase. Different from Uhrenius [106], the λ-Fe_2W was added to the study, and the μ phase was also adopted as Fe_7W_6. Since there are few thermodynamic data for Fe_6W_6C and FeW_3C, these phases have not been reported to participate in solid–liquid equilibrium. Raghavan [108] redrawn the calculated isothermal sections at 1320 °C and 1500 °C based on Gustafson's work [107]. Fe_3W_3C (M_6C) is present between 1320 and 1500 °C. Tang et al. [109] successfully prepared shielding material Fe–W–C alloy with different W contents and high density by using powder metallurgy processes. In addition, Eryomina et al. [110, 111] also prepared $(Fe, W)_6C$ and $(Fe, W)_{12}C$ carbides with high hardness and wear resistance. In addition to the phases mentioned in the phase diagram of Fe–W binary alloys, the new phases that appear in the Fe–W–C ternary system are mainly composed of WC, $(Fe, W)_6C$, $(Fe, W)_{12}C$ and $M_{23}C_6$.

Some studies have been conducted on Fe–W–Cr systems [112, 113]. Yin et al. [114] simulated the effects of different alloying elements on the precipitation of $M_{23}C_6$ particles in ferritic steels, as shown in Fig. 9. When W is added to the

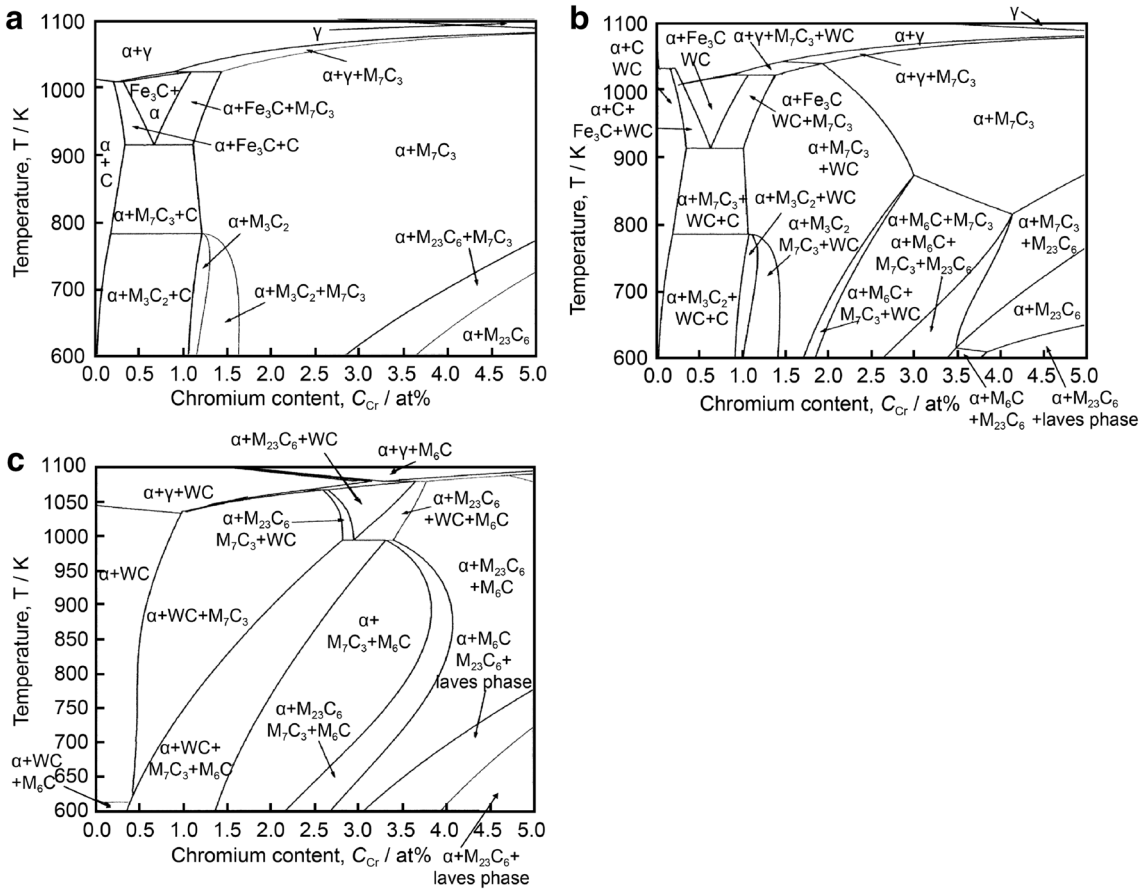

Fig. 9 Fe–Cr system phase diagrams calculated using MTDATA at 0.693 at.% carbon and with the addition of **a** 0 at.% W, **b** 0.1 at.% W, **c** 0.7 at.% W. Reproduced with the permission from Ref. [114]. Copyright 2003 Elsevier

system, two new phases appear in the range of temperature and composition of interest, namely M_6C and WC. M_6C appears at higher chromium concentrations, WC covers a wide range of chromium concentrations, and the appearance of these two phases appears to have little effect on the formation of chromium carbide. However, when the W content reaches about 0.6 at.% (~2.0 wt.%), the phase diagram changes significantly, as shown in Fig. 9c. First, due to the higher concentration of W, most of the carbon appears to enter the WC phase and the graphite present in the low W content system disappears. Second, the cementite vanishes as tungsten absorbs the majority of the available carbon. Finally, M_6C is formed at low chromium concentrations and low temperatures. The combined effect is to push the boundary between the (α-Fe + WC) and (α-Fe + WC + M_7C_3) phase fields to a higher chromium content to delay the formation of chromium carbide. As the W content increases, the phase boundary is pushed to the higher chromium content. This results in a sharp increase in the equilibrium chromium concentration in the matrix. In addition, Liu et al. [115] studied the microstructure evolution of three G115 steels [9Cr- (2.3, 2.6, 3.0) W-3Co (wt.%)] under different aging times at 675 °C, mainly martensitic laths, dislocations and precipitates. The results show that the coarsening rate of lath and Fe_2W particles increases with the increase of W concentration during thermal aging, and the dislocation density and particle density decrease rate of Fe_2W particles increases with the increase of W concentration.

Niewolak et al. [116] investigated the microstructural features of three Fe-22Cr wt% model steels with W additions between 2.5 and 7 wt.% after long-term exposures in the temperature range 650–900 °C. The composition of intermetallic phases formed at different temperatures was calculated by Thermocalc software and compared with the experimental results. As shown in Fig. 10, there are three phases in the Fe–Cr–W system: ferrite matrix, λ phase, σ phase and χ phase precipitates. The σ phase precipitation is a binary intermetallic compound in the Fe–Cr system, and its basic composition is FeCr. The composition of the λ phase is $(Fe, Cr)_2$ W. The χ phase is a complex ternary phase with an α-Mn structure that appears in the Fe–Cr–W ternary system [112, 117]. The approximate chemical formula of the χ phase can be written as Fe_5Cr_3W. It can be seen from Fig. 10 that the calculations in the temperature

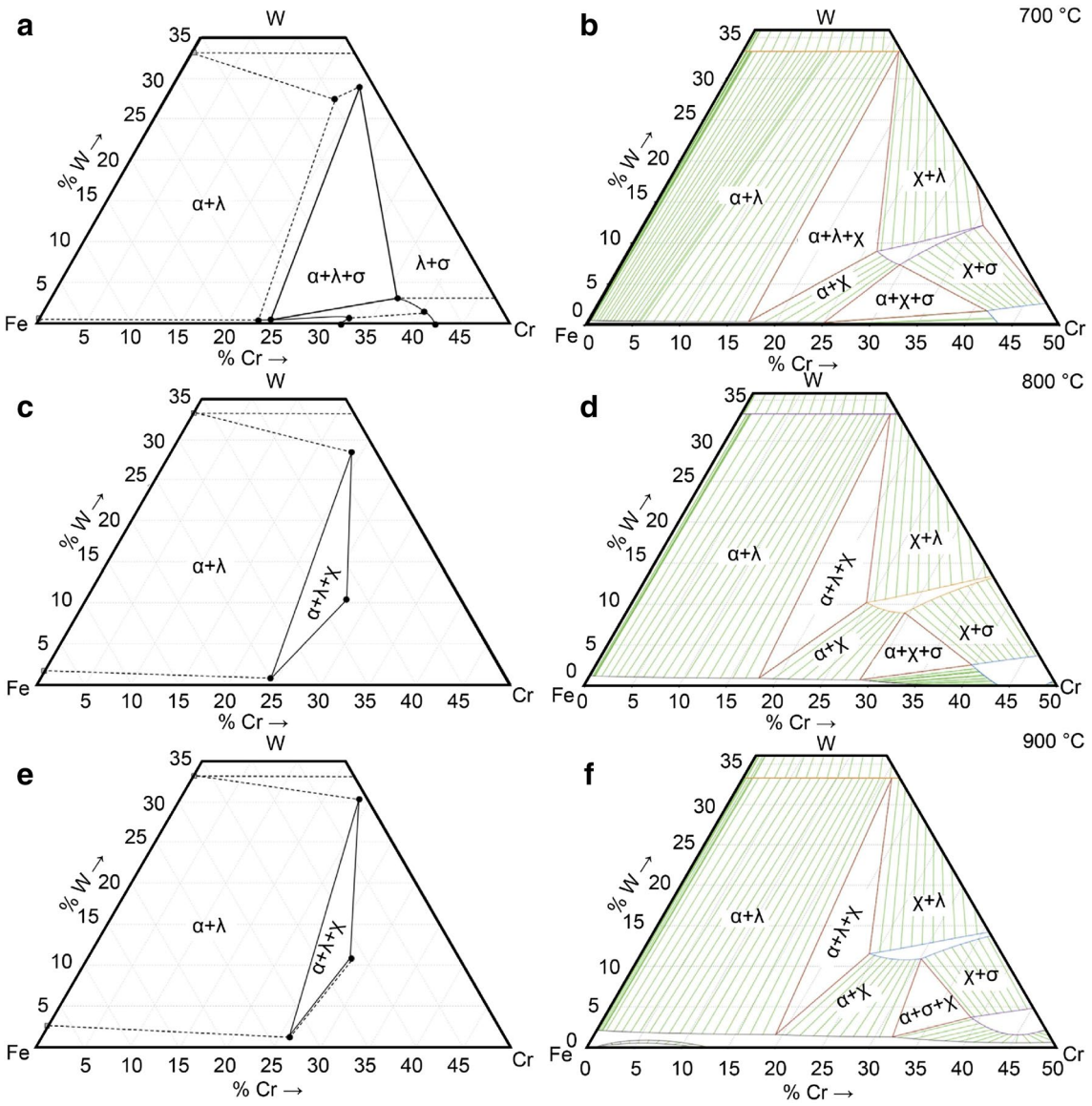

Fig. 10 Part of ternary Fe–Cr–W phase diagrams **a**, **c**, **e** from experiments and **b**, **d**, **f** calculated with ThermoCalc software at 700–900 °C. Reproduced with the permission from Ref. [116]. Copyright 2017 Elsevier

range of 800–900 °C give a qualitatively correct description of the phases present in the microstructure. However, there are significant differences between calculations and experiments at 700 °C. First, the presence of the χ phase in the alloy exposed to 700 °C, predicted by Thermocalc, was not observed in the experiment. This is unexpected because the χ phase is relatively easy to form in ferritic steel and precedes other phases (such as the σ phase), indicating that the χ phase does not exist at $t \leq 700$ °C in the range of components studied. The second important inconsistency between calculations and experiments is that the theoretical stoichiometric ratio of the λ-Fe_2W phase has a large deviation, especially in terms of the possession of the tungsten position. According to Thermocalc the λ-$(Fe, Cr)_2$ W contains 33.3 at.% tungsten, indicating that only tungsten occupies the corresponding sites. However, the measured tungsten concentration range of 25.6 at.%–32.8 at.% indicates iron occupies a relatively large tungsten position. Third, the positions of the two-phase α–σ field are inconsistent.

In addition, other ternary alloy phase diagrams have been studied in some literature [118–120], and the number of studies in this area is increasing. With the continuous development of simulation software and more accurate testing methods, it is necessary to study this in more depth so that the microstructure of alloy steel can be accurately controlled.

4 Effect of tungsten on mechanical properties

4.1 Effect of tungsten on tensile strength

The tensile test is a test method to determine the properties of materials under axial tensile load. The data obtained from the tensile test can be used to determine the elastic limit, elongation, elastic modulus and many other tensile properties of the material. The results by Zhao et al. [91] show that the addition of W increases both yield strength and ultimate tensile strength at the expense of strain, as shown in Table 2. When the W content increases from 0 to 0.5 wt.%, the microstructure changes from polygonal ferrite (PF) and pearlite to a mixture of allotriomorphic ferrite and acicular ferrite (AF), as shown in Fig. 11 [91]. According to Yang [121], with the growth of AF, the dislocations generated are inherited by AF, and the dislocation density is usually 10^{14} m^{-2}, which contributes some 145 MPa to its strength. When the W content increases to 1 wt.%, the microstructure is mixed with AF and a small amount of bainite. When the W content is increased to 2 wt%, the microstructure is dominated by bainite. The dislocation density of bainite is about 4×10^{14} m^{-2} [122], which is higher than that of the allotriomorphic ferrite with $\rho_d \approx 0.5 \times 10^{14}$ m^{-2} in the same steel. In another supporting experiment, the dislocation density of bainite and allomorphic ferrite were measured to be 1.7×10^{14} and 0.37×10^{14} m^{-2}, respectively [123]. Bainite contains more dislocations than ferrite, which improves tensile strength. The reasons for the strength increase after the addition of W are also considered as follows: first, the solid solution strengthening is caused by the addition of W, because the atomic size of W is about 10% larger than that of Fe. Second, the hardening is caused by fine precipitates in W-containing steel. With the refinement of various

Table 2 Tensile properties of the as-forged specimens [91]

Specimen (W)	Yield strength (MPa)	Ultimate tensile strength (MPa)	Strain (%)
0	363.2	592.7	29.4
0.5	382.7	645.0	22.9
1	400.5	706.1	21.9
2	414.3	751.7	20.8

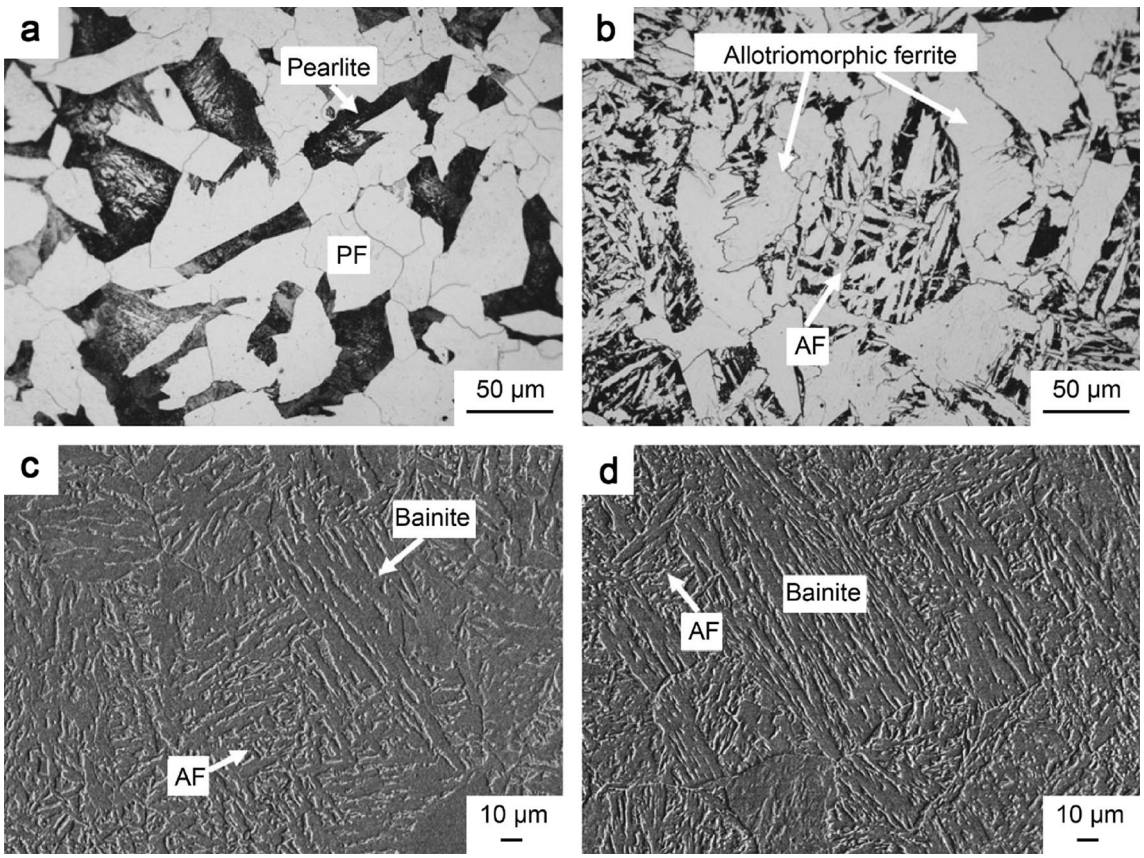

Fig. 11 **a**, **b** OM and **c**,**d** SEM structures of the as-forged specimens: **a** 0 W, **b** 0.5 W, **c** 1 W, **d** 2 W. Reproduced with the permission from Ref. [91]. Copyright 2013 Elsevier

precipitates, the obstacles to dislocation movement increase with the increase of the interface between the phases, resulting in an increase in strength. Figure 12a, b [91] show the characteristics of the precipitated phase in samples 0 and 2 wt.% W during forging. It can be seen that the addition of W significantly refines the precipitated phase, thus improving the tensile strength of the alloy.

Jung et al. [124] prepared five kinds of heat-resistant austenitic SSs with different contents of W and Mo. In the absence of Mo, the strength of the alloy steel increases with the addition of W content due to the increase of M_7C_3 carbides. When W is added combined with Mo, the strength of samples mixed with 1 wt.% W and 1 wt.% Mo alloy steel can be found to be greater than that of samples with 2 wt.% W. Salama et al. [125] developed a series of tungsten austenitic SS alloys by exchanging Mo with W in standard SS316. It is shown that the strength of the alloy steel first increases with increasing W content. The strength reaches a maximum and then decreases when W/(W + Mo) equals 0.74. When Mo is completely replaced by W, the strength of the steel decreases to the level where only molybdenum is added to the alloy steel. This behavior is mainly attributed to the fact that composite W–Mo carbides have a higher hardening effect than single Mo- or W-carbides.

In summary, tungsten improves the strength of alloy steel, which can be attributed to grain refinement, solid solution hardening of tungsten and the high strengthening effect of W–Mo complex carbides. Therefore, the improvement of the strength of alloy steel can be considered to add W and Mo in a certain ratio, which at the same time can save the cost of expensive alloying elements [126].

4.2 Effect of tungsten on compressive strength

Alloy steels are widely used as a structural material in thermal power and nuclear power plants [85]. The steels must have good compressive strength. Chen et al. [127] fabricated high-density W–Fe composites with different W contents by laser metal deposition. W powder (99.9% purity) and aerosolized Fe powder (99.9% purity) were used in this study. The composition of the mixed powders before printing was 21 wt.%, 46 wt.%, 68 wt.% and 86 wt.% W (remainder Fe) and were denoted as 21 W–Fe, 46 W–Fe, 68 W–Fe and 86 W–Fe, respectively. The compressive stress–strain curves of tungsten iron composites with different W compositions are shown in Fig. 13 [127]. It should be mentioned that the compression experiment is stopped when the strain value is 50% because the maximum force of the experimental equipment was set at 50 kN. The minimum yield strength of 21 W–Fe is 1250 MPa, and there is no sign of failure edge when the compression strain is 50%. Therefore, 21 W–Fe has excellent ductility. The experimental results show that with the increase of

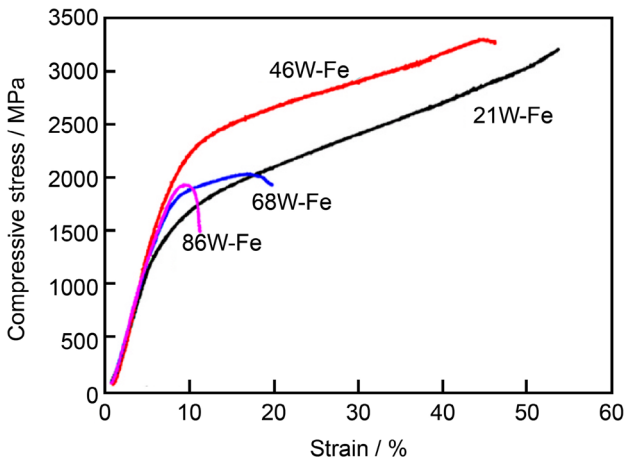

Fig. 13 Compressive stress–strain curves of the W–Fe composites. Reproduced with the permission from Ref. [127]. Copyright 2021 Elsevier

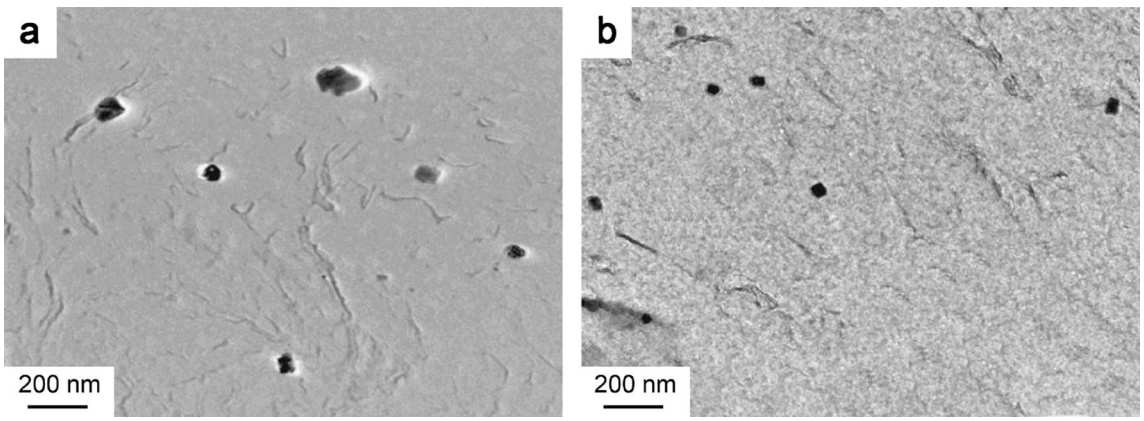

Fig. 12 Characteristic of precipitates in the as-forged, **a** 0 W, **b** 2 W specimens. Reproduced with the permission from Ref. [91]. Copyright 2013 Elsevier

W content, the compressive strength of W–Fe composites first increases and then decreases, while the plasticity decreases gradually. The 46 W–Fe composites exhibit excellent comprehensive mechanical properties with a maximum yield compressive strength of about 1710 MPa. Because of the high-volume percentage of finely dispersed Fe_2W nanoparticles in 21 W–Fe and 46 W–Fe, W–Fe composites have high strength. Tungsten-iron composites containing 35 wt.%–60 wt.% W is characterized by the honeycomb structure of nanoparticles, which is considered to be beneficial to crack suppression and ductility improvement [128–130]. However, more intermetallic compounds Fe_7W_6 are produced in 68 W–Fe and 86 W–Fe. Fe_7W_6 is a hard phase, but it is brittle. The rough-layered structure of the Fe_7W_6 phase often leads to poor mechanical properties. However, when the size of the Fe_7W_6 phase is in the range of 0.3–1 μm, it has been shown to increase the compressive strength of the alloy steel [131].

Therefore, the addition of an appropriate amount of W to alloy steel can be considered to improve the compressive strength of alloy steel through fine grain strengthening and precipitation strengthening. However, the addition of W to alloy steel should avoid the formation of coarse brittle metal compounds. Otherwise, it will cause a decrease in compressive strength and ductility.

4.3 Effect of tungsten on hardness

Hardness is the ability of a material to resist local hard material pressed into its surface. Zhao et al. [92] investigated the effect of different W contents (0, 0.1 and 1 wt.%) on the hardness of microalloyed steel at different cooling rates. The relationship between hardness and cooling rate is presented in Fig. 14 [92]. It can be found that the hardness of microalloyed steel increases with the increase of W content at a given cooling rate. This is attributable to the fact that adding W lowers the martensitic transformation temperature while increasing hardness [132]. However, when the cooling rate is close to 0.1 °C·s^{-1} and 120 °C·s^{-1}, the hardness difference of microalloyed steel with different W contents gradually decreases, which is caused by the consistency of the microalloyed steel phase. In this regard, Zhao et al. [92] established the relationship between hardness and cooling rate using an exponential equation [133]. The exponential equation is as follows:

$$HV = a + b \times \exp(c \times v) + d \times \exp(e \times v), \quad (1)$$

where HV is Vickers hardness (HV2), v is the cooling rate (°C), a, b, c, d and e are constants. The expressions of hardness and cooling rate were obtained by regression analysis. Figure 14 shows the comparison of hardness values

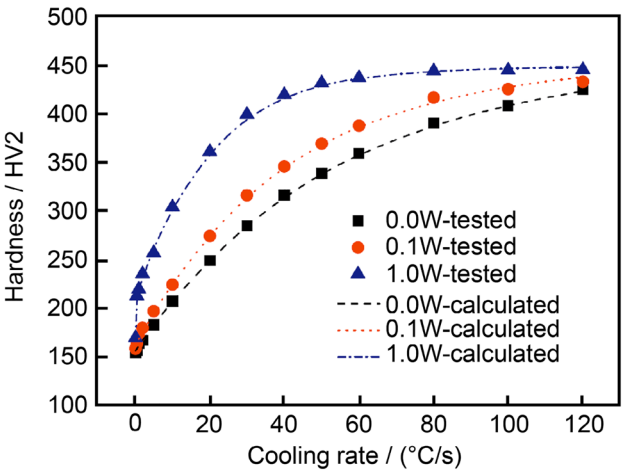

Fig. 14 Dependence of hardness on cooling rate of the microalloyed steel. Reproduced with the permission from Ref. [92]. Copyright 2013 Elsevier

measured and calculated at different cooling rates. It can be seen that the calculated results agree well with the experimental results.

Chen et al. [127] studied the effect of W on α-Fe hardness by laser metal deposition. The compositions of the experimental powders were 21 wt.%, 46 wt.%, 68 wt.% and 86 wt.% W (the remainder was pure Fe). It was found that with the increase of W content, the average hardness of W–Fe composites increased continuously. Since the prepared composites contain a lot of unmelted tungsten powder, which is harder than Fe. In addition, the formation of fine and dispersed Fe_2W nanoparticles in the W–Fe composite improves the overall mechanical properties of the material. Although Fe_7W_6 is brittle, it is a hard phase, which also increases hardness.

Zhang et al. [134] studied the effect of W on the hardness of austenitic heat-abrasion resistant steel. The reason for the increase in hardness is that high hardness MC carbides are dispersed in the grain interior and grain boundary. With the increase of W content, the content of carbide increases. Salama et al. [125] developed a series of W-containing austenitic SSs by exchanging Mo in standard SS316 with W. It was found that the hardness of samples increases with the increase of W/(W + Mo). The increase in hardness may be attributed to the solid solution hardening of tungsten and the higher strengthening effect of complex W–Mo carbides as compared with molybdenum carbides. However, the high reduction amount of W instead of Mo content leads to a decrease in hardness. This is caused by composite W–Mo-carbides having a higher hardening effect than single Mo- or W-carbides. The same conclusion was obtained in other literature about W enhancing the hardness of austenitic steel [135, 136].

Chen et al. [137] added different amounts of tungsten powder (0.07%, 0.4%, 0.6%, 0.8% and 1%, in wt.%) to H13 die steel and sintered by microwave. As the W content increases, the hardness of the samples increases continuously, owing to the grain refinement with the increase of W content. In addition, W-carbide precipitation also improves the hardness of the alloy. Similar conclusions have been obtained in other literature about W enhancing the hardness of martensitic steel [87].

Lv et al. [138] studied the effects of tungsten on the microstructure and properties of high-chromium cast iron. The as-cast microstructure of high chromium cast iron shows the typical hypereutectic microstructure, which is mainly composed of refined hexagonal-shaped primary M_7C_3 and eutectic carbides in a matrix of austenite and a small amount of martensite. The experimental results show that with the increase of W content from 0 increased to 2.75 wt.%, the hardness of the sample also increases gradually. This is attributed to the positive effect of a solid solution of tungsten in the matrix on the hardness of the matrix. Similar results have been reported in the literature [139]. The matrix microhardness of all samples containing tungsten is higher than that of samples without tungsten. Furthermore, the addition of W refines the matrix and improves the microhardness of the matrix. With the increase of the amount of W, more W carbides are formed and dispersed in the matrix, which is also beneficial to improving the strength of the alloy.

Conclusively, the addition of W increases the hardness of the alloy steel. The increase in hardness is attributed to dispersion strengthening, grain boundary strengthening, solid solution strengthening and the formation of W carbides. Although the addition of W leads to a continuous increase in hardness, it also leads to a decrease in other properties of the alloy steel. In practice, it is necessary to consider all other properties while increasing the hardness to meet the production needs.

4.4 Effect of tungsten on impact toughness

Impact toughness refers to the ability of a material to absorb plastic deformation work and fracture work under impact load, reflecting the impact resistance of the material. The impact toughness of steel is affected by chemical composition, heat treatment status, smelting method, internal defects, processing technology and ambient temperature. This section mainly studies the effect of tungsten on the impact toughness of alloy steel.

Zhao et al. [91] prepared four kinds of microalloyed forged steels with different W additions (0, 0.5 wt.%, 1 wt.% and 2 wt.%). Heat treatment is carried out at the temperature ranging from 840 to 950 °C, followed by air and furnace cooling [91]. The relationship between impact energy and heat treatment temperature under air and furnace cooling conditions is shown in Fig. 15. The impact energy decreases with the increase of W content in both air and furnace cooling conditions. The addition of W increases the hardenability and promotes the formation of bainite [140]. Since bainite is beneficial for improving strength, but not for increasing ductility compared to ferrite. The crack extends undeviatingly across the bainite during the cleavage failure [141]. Therefore, the addition of W decreases the impact toughness of the microalloyed steel.

Salama et al. [125] prepared a series of tungsten austenitic SS by replacing Mo with W. The results show that the impact properties will be reduced by replacing Mo with W. This is related to the brittleness effect of W–Mo-carbides. Zhang et al. [142] studied the impact toughness of W on Mo-free SS. The impact toughness decreases with the increase of W content. It was found that the fracture mode changes

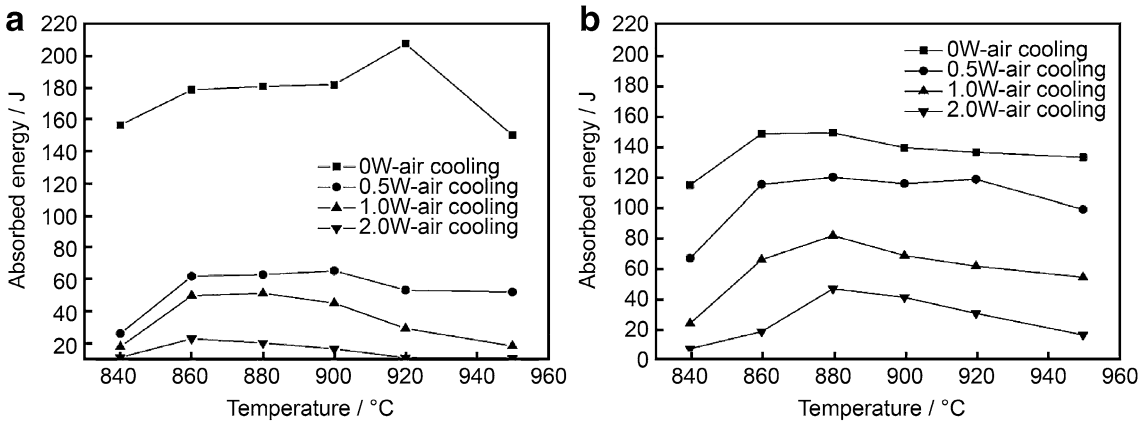

Fig. 15 Dependence of impact energies on temperatures under, **a** air and **b** furnace cooling conditions. *Note*: The impact energies of the as-forged specimens are 19.3, 14.5, 10.6 and 9.8 J for 0 W, 0.5 W, 1 W and 2 W specimens, respectively. Reproduced with permission from Ref. [91]. Copyright 2013 Elsevier

from ductile fracture to brittle fracture with the increase of W content. In addition, the increase of W content results in a small amount of martensite in steel, reducing the impact toughness.

Lv et al. [138] studied the effect of tungsten on the impact toughness of high chromium cast iron. The results show that the matrix of high chromium cast iron transforms from austenite to lath martensite after heat treatment with W content ranging from 0 to 1 wt.% and a small amount of residual austenite also exists. At this time, the impact toughness is improved because the solid solution in the matrix significantly increases the microhardness of the matrix. When the W content exceeds 1 wt.%, the isolation of the excessive carbides precipitated in the matrix has a detrimental influence on the impact toughness.

Jin et al. [13] studied the effect of W content and heat treatment on the impact toughness of Fe-11Cr-10Ni-xW-0.4Al-0.3Ti stainless maraging steels. The impact toughness decreases when the tungsten content increases from 2 to 5 wt.%. It is also found that the Charpy impact energy is very sensitive to the existence of the Fe_2W. The Charpy impact energy decreases sharply with the increase of W content, mainly because the number of Fe_2W formed during solution treatment increases. Sakasegawa et al. [143] reached the same conclusion in their study and found that the interface between Fe_2W and the matrix is the site of crack nucleation because Fe_2W is incoherent with the matrix. The sites of crack generation increase with the increase of Fe_2W, and these precipitation morphologies reduce the toughness.

Miyahara et al. [144] studied the effect of W on the impact toughness of 10 wt.% Cr ferritic SS. It was found that the material changes from the martensite phase to ferrite and martensite mixture with the increase of W content, and the proportion of ferrite increases with the increase of W content. Fe_2W is prone to precipitate in the δ-ferrite, which leads to a decrease in toughness [145, 146].

To conclude, the addition of W decreases the impact toughness of the alloy steel. The main reason for the decrease in toughness is the transformation of microstructure in the alloy steel caused by the addition of W or the presence of Laves phase Fe_2W. Therefore, in the addition of W content to increase the strength of alloy steel at the same time need to consider the decline in toughness to prevent safety accidents.

4.5 Effect of tungsten on creep behavior

Creep is the phenomenon that a metal material will slowly produce plastic deformation with the increase of time, even if the stress is less than its yield strength under a certain temperature and a long-term stress state. Jang et al. [147] investigated the effect of the combined addition of W and Mo on the creep properties of alumina-forming austenitic (AFA) heat-resistant steels. The creep-strain curves of AFA steel and W-added alumina-forming austenitic (AFA_W) steel at 700 °C under 160 MPa are shown in Fig. 16a [147]. Figure 16b shows the log–log plots of the creep rate versus time curves for the AFA and AFA_W steels. The results show that the creep rupture strength increases with the increase of W content. The finer and denser distribution of the Fe_2W contributes to improving the creep properties of AFA_W steels through precipitation strengthening, as shown in Fig. 17. In addition, the combined addition of W and Mo seems to have a more significant effect on the precipitation of Fe_2W. On the one hand, the enthalpy of the formation of Fe_2(W, Mo) is lower than that of Fe_2Mo due to the addition of W. On the other hand, it is related to the influence of coarsening rate. The coarsening rate is usually expressed by Ostwald ripening rate.

$$R^3 - R_0^3 = 8\gamma C_\infty v^2 DT/9R_gT, \tag{2}$$

where R is the precipitation radius at time t, R_0 is the precipitates radius at time 0 and γ is particle surface tension or

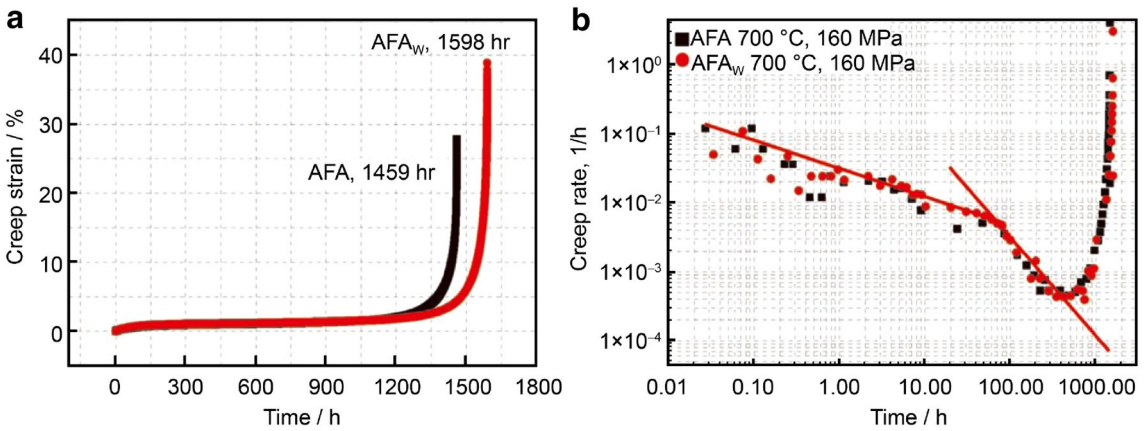

Fig. 16 **a** Creep rupture time versus creep strain curves, **b** creep rate versus time in log–log plots for AFA and AFA_W steels at 700 °C. Reproduced with the permission from Ref. [147]. Copyright 2015 Elsevier

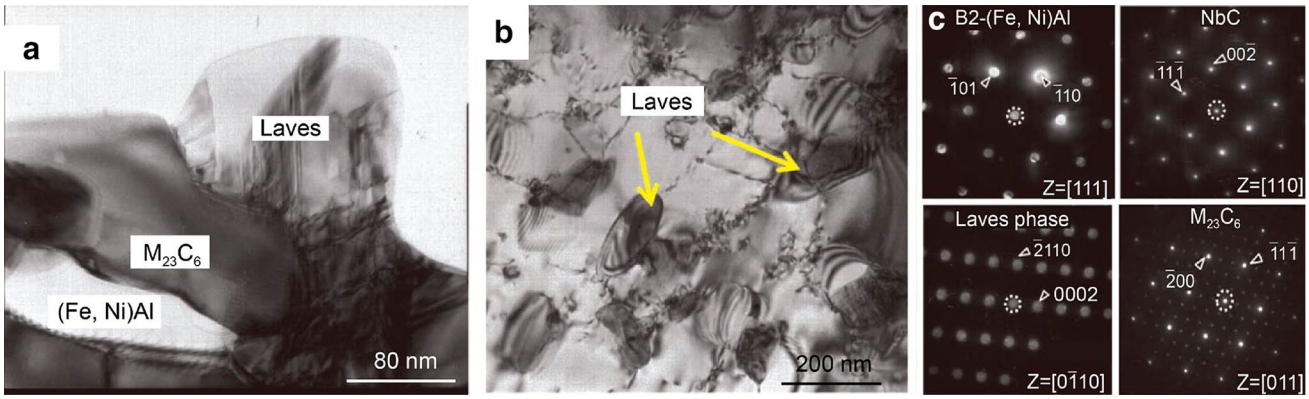

Fig. 17 TEM microstructure of crept AFA_W steel, and selected area diffraction patter analysis results of crept AFA_W steel; **a** precipitates at grain boundary, **b** those within the grain, **c** the selected area diffraction patterns of precipitates in AFA_W steel. Reproduced with the permission from Ref. [147]. Copyright 2015 Elsevier

surface energy, $C\infty$ is the solubility of the particle material, ν is the molar volume of the particle material, D is diffusion coefficient of the particle material, R_g is the ideal gas constant, T is the absolute temperature and t is time. The coarsening behavior of particles is closely related to solubility and diffusivity of alloying elements in the second phase according to Ostwald ripening equation. The coarser kinetics of Fe_2W in AFA_W steel is slower than that in AFA steel. Considering all these reasons, the combined addition of W and Mo has a positive effect on the size and fraction of Fe_2W precipitation in AFA_W steel. The increase of the volume fraction of the fine Fe_2W enhances the precipitate hardening effect and ultimately improves the creep properties of AFA_W steel.

Abe [148] studied the creep deformation behavior of tempered martensitic steel. The results show that the creep rupture strength increases with the increase of W content. The precipitation of Fe_2W effectively reduces the minimum creep rate, while the coarsening of Fe_2W accelerates the creep rate after reaching the minimum creep rate [149]. Transient creep is the result of excess dislocation movement and annihilation, whereas accelerated creep is the result of a gradual loss of creep strength due to microstructural evolution, such as precipitation aggregation and martensitic lath coarsening [150]. The lath coarsening rate decreases with the increase of W content, which is related to the Ostwald ripening rate of $M_{23}C_6$ carbide. Fedoseeva et al. [33] studied the coarsening behavior of Fe_2W in 10% Cr-3% Co-3% W (wt.%) steel during both creep and aging at 923 K. The depletion of W solute in the ferrite matrix is accompanied by the precipitation of the Fe_2W in which both processes are accelerated by creep strain. The Fe_2W grains grow independently at the lath boundary and the high-angle boundary of the block, inclusions and prior austenite grains. The Fe_2W particles located on the high-angle boundary are easy to coarser, resulting in the formation of particles with sizes > 200 nm. The dense Fe_2W chains along the lath boundary contribute significantly to the creep behavior. Overall, the addition of W enhances the creep resistance of the alloy steel due to the contribution of Fe_2W precipitation to the creep behavior.

4.6 Effect of tungsten on low cycle fatigue

Under the action of cyclic stress and strain, the material gradually produces local permanent cumulative damage in one or several places, and cracks or sudden complete fractures occur after a certain number of cycles. Fatigue can be divided into high cycle fatigue (HCF) and low cycle fatigue (LCF) according to the number of cycles experienced before material failure and the stress level of the fatigue load.

1. HCF. The stress level acting on the parts and components is low, and the number of failure cycles is generally higher than the fatigue of 10^4, such as springs and transmission shafts.
2. LCF. The stress level acting on the parts and components is high, and the number of failure cycles is generally lower than the fatigue of 10^3–10^4, such as the fatigue of pressure vessels and gas turbine parts.

Steel has excellent plasticity and ductility. There are few reports on the effect of W addition on the HCF of steel. Ferritic/martensitic steels with chromium content between 9 wt.% and 12 wt.% have better creep resistance and excellent thermal properties. Therefore, many scholars have studied the LCF of tungsten added to this steel.

Park et al. [7] studied the LCF properties of 9Cr-1Mo steel with four different W contents (0, 1.2, 1.8 and 2.7 W) at 298 K and 873 K. The results show that LCF life increases with increasing W content when W content is below 1.8 wt.%. However, the LCF of the alloy decreases at the content of 2.7 wt.% W. Typically, fatigue

crack initiation accounts for most of the fatigue life at low strain amplitudes, while propagation processes account for most of the total life at high strain amplitudes [151]. Therefore, ductility plays an important role at higher strain amplitudes, while strength is an important variable to be considered at lower strain amplitudes. When W is below 1.8 wt.%, fatigue life increases with strength and ductility, thus 1.8 W has the best fatigue life. However, when the W content reaches 2.7 wt.%, although its strength and ductility are the highest, its LCF deteriorates. Since soft δ-ferrite grains are formed along the original austenite grain boundaries at a W content of 2.7 wt.%, no δ-ferrite grains are found in the other specimens. δ-ferrite grains are much softer than the matrix, and under cyclic loading, deformation is concentrated in the soft δ-ferrite, which leads to an acceleration of fatigue crack initiation and consequently to a decrease in its LCF. Therefore, the LCF of 2.7 W alloy steel deviates greatly from the trend of increased LCF with the addition of W.

Shankar et al. [152] investigated the effect of W on the LCF of reduced activation ferritic/martensitic (RAFM) steel. Four kinds of laboratory steels were used in the study, as shown in Fig. 18 [152]. These steels are designated as 1 W–0.06Ta, 1.4 W–0.06Ta, 2 W–0.06Ta and 1 W–0.14Ta, respectively. At 823 K and 3×10^{-3} s^{-1} strain rates, the addition of W can improve the LCF of RAFM compared with 9Cr-1Mo steel. The LCF of RAFM steel is improved when the addition of W is increased from 1 wt.% to 1.4 wt.%. With a further increase in W from 1.4 wt.% to 2 wt%, the LCF of RAFM steel is improved, but the amount of softening deteriorates. This means that increasing W to 1.4 wt.% is beneficial, but a further increase to 2 wt.% is detrimental. Therefore, 1.4 W-0.06Ta

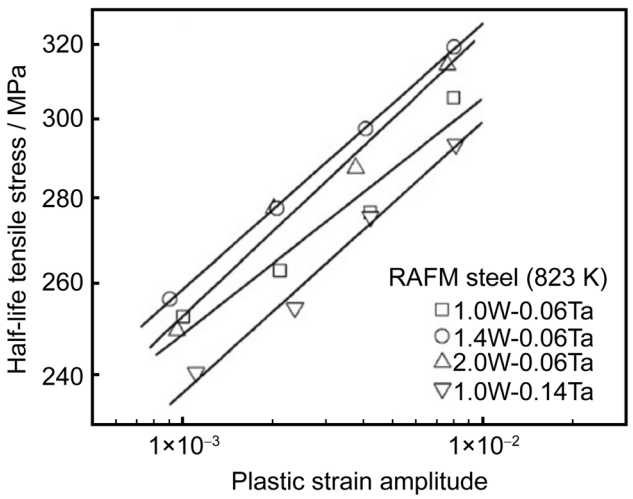

Fig. 18 Effect of tungsten and tantalum on cyclic stress–strain curves of RAFM steels at 823 K and strain rate 3×10^{-3} s^{-1}. Reproduced with the permission from Ref. [152]. Copyright 2012 Elsevier

is a better choice for long-term prospects. In addition, the present study found that the addition of Ta increases fatigue life by an order of magnitude compared with the addition of W. It also provides a new direction for improving fatigue life in the future. Laha et al. [28] came to a similar conclusion. With the increase of W content, the refinement of the martensite substructure can improve the microstructure stability of RAFM steel [153], which is considered to be the reason for the increase in LCF of steel with the increase of W content.

It can be concluded that the addition of W can improve the LCF to some extent, but it does not improve continuously with the increase of W content. Furthermore, the addition of other elements can also improve the LCF of alloy steel, such as Ta. Regarding the mechanism of the synergistic effect of W and other elements to improve the LCF further research is needed.

5 Effect of tungsten on corrosion resistance

When alloy steel is used in certain environments (such as seawater), it can cause serious problems due to corrosion, including failure of steel parts, leakage of pipes and collapse of buildings, leading to significant economic losses. Therefore, alloy steel that can resist corrosion is needed in practical industrial production. This type of alloy steel is also known as SS. The most critical element in SS is Cr, and the corrosion resistance of SS can be attributed to the presence of a "passivation film" on the metal surface, which is typically 1–3 nm thick [154].

The main form of corrosion that occurs in SS is pitting corrosion. In addition to Cr elements, the addition of small amounts of Mo [155], N [156], W [157], V [157] and Cu [158] has been reported to significantly increase the pitting resistance of SS. The combined effect of these alloying elements can be obtained from the pitting resistance equivalent number (PREN) [159–161]. The most common formula for calculating PREN is as follows[162]:

$$\mathrm{PREN} = w_{\mathrm{Cr}} + 3.3\left(w_{\mathrm{Mo}} + 0.5w_{\mathrm{W}}\right) + 30w_{\mathrm{N}} \quad (3)$$

where w_{Cr}, w_{Mo}, w_{W} and w_{N} are the mass percent of Cr, Mo, W and N elements in the austenite phase, respectively. The larger the value of PREN means the better the corrosion resistance of SS. However, this equation only considers the alloying elements in solid solution and neglects the effect of the precipitated phases.

It can be seen in the equation that W can improve the corrosion resistance of SS, and many studies have shown that the addition of W can improve the corrosion resistance of SS. The corrosion potential of W in 1 N HCl at 60 °C is −0.10 V versus SCE (Saturated calomel electrode), which

is much higher than the corrosion potential of 16Cr–14Ni steel (−0.37 V) [163]. However, pure W itself does not form a protective layer [163]. Therefore, the mechanism of the W to improve the corrosion resistance of SS has been widely studied.

Based on the microstructure of SSs which varies by composition and processing, SSs are divided into the following four main groups: austenite, ferrite, duplex and martensite [164, 165]. Bui et al. [163] investigated the effect of W in acidic and neutral chloride-containing electrolytes on the corrosion passivation of austenitic SSs. It was found that the corrosion resistance of the SS increases significantly with the increase of W content. Under the same conditions, tungstate ions in neutral chloride solutions also inhibit pitting corrosion by polarization studies of 16Cr–Ni steel in tungstate ion solutions at different concentrations. The results indicate that in acidic media, W interacts with water to form an insoluble WO_3. Under neutral pH conditions, WO_3 binds to the substrate and improves the stability of the passivation film, resulting in corrosion inhibition [163].

Ahn et al. [166] studied the effect of W on the corrosion resistance of Fe–29Cr ferritic SSs. The anodic polarization curves of Fe–29Cr–*y*W ($y = 0$–8 wt.%) alloy at 80 °C in 4 M $MgCl_2$ solution are shown in Fig. 19 [166]. The pitting potential of SS increases with increasing W content. By measuring the anodic polarization response in chloride or acidic solutions, it was found that with increasing W content, the pitting potential in the passivation zone of the alloy increases, and the primary passivation potential and critical anodic current density decrease. This indicates that the addition of W improves the corrosion resistance of SS. It can be determined that the addition of W enhances the stability of the passivation film. The improved corrosion resistance of W is attributed to the delayed formation of the σ-phase after the addition of W. The conclusions of Bui et al. [163] are also adopted. However, the exact mechanism has not been confirmed by further experiments.

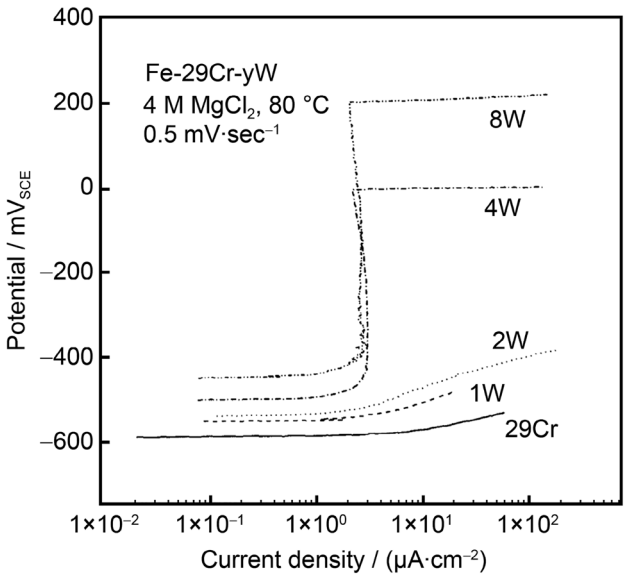

Fig. 19 Anodic polarization curves for Fe–29Cr ferritic SSs containing 0 to 8 wt.% of tungsten in 4 mol·L^{-1} $MgCl_2$, solution at 80 °C. Reproduced with the permission from Ref. [166]. Copyright 1998 Elsevier

Duplex stainless steel (DSS) is mainly composed of balanced austenite and ferrite. In nitrogen-containing DSS, nitrogen is mainly solid-soluble in the austenitic phase, so the corrosion resistance of the austenitic phase is better than that of the ferrite phase [142]. W is a strong ferrite former and the corrosion resistance of ferrite increases with the increase of W content, thus improving the corrosion resistance of DSS.

Park et al. [167] investigated the effect of aging on W-containing DSS and found that the corrosion resistance of the alloy decreases with aging at 475 °C in the absence of W. However, the degradation of the corrosion resistance of the DSS with the addition of W is retarded. W diffuses slowly during the aging decomposition of the ferrite phase and hinders the diffusion of other elements during aging, thus slowing down the precipitation of the Cr-rich α' phase. Therefore, the addition of W leads to the improvement of the corrosion resistance of DSS.

The effect of W on the corrosion resistance of super duplex SS was studied from the perspective of precipitation kinetics by Torres et al. [168]. Super SS is high-alloy SS containing high Ni, Cr and Mo. They found that the addition of W retards the precipitation of the Cr-rich σ phase but promotes the nucleation of the χ phase. Both σ and χ phases reduce the corrosion resistance of super duplex SS, but the critical pitting temperature is reduced more when the σ phase is the main precipitation phase. Therefore, the addition of W improves the corrosion resistance of super duplex SS.

The effect of adding W and Cu on the corrosion resistance of martensitic SSs was investigated by Li et al. [169]. The results show that super-martensitic SSs containing W and Cu have better pitting corrosion resistance than super-martensitic SSs without W and Cu under the same conditions. However, their study lacks the experimental study of W as the only variable on the corrosion resistance of martensitic SSs.

In summary, the addition of W improves the corrosion resistance of alloy steel. The main roles of W in alloy steel are (1) enhancing the stability of the passivation film and (2) delaying the reduction of the precipitation of harmful phases. However, further studies are needed on the mechanism of action of how W improves the corrosion resistance of alloy steel.

6 Effect of tungsten on hydrogen embrittlement

With the advancement of science and technology, the demand for oil and gas energy is increasing. Therefore, there is a need for alloy steel that combines high strength and excellent HE resistance. However, some studies have pointed out that high-strength steel is susceptible to HE, and its sensitivity to HE increases with the increase of strength and is affected at much higher hydrogen concentrations [170, 171]. When hydrogen is present in the steel, the ductility of the steel decreases and unpredictable failure may occur [172, 173], which will cause unimaginable disaster. HE is the phenomenon of hydrogen penetrating steel and causes steel to fail below its yield stress. Various forms of HE have been explained by the following four theories: (1) internal hydrogen pressure, (2) lattice de-cohesion, (3) hydrogen-enhanced plasticity or dislocation interactions, (4) hydride formation [174].

There are two main sources of hydrogen in alloy steel as follows:

1. Hydrogen absorbed by alloy steel during melting, welding, or other processing technology.
2. Hydrogen introduced by alloy steel in a service environment.

The hydrogen from the case I can be removed from the steel by heat treatment, while the latter is difficult to eliminate. Therefore, a large number of studies have been carried out on HE of high-strength steel in various environments, such as stress corrosion cracking in aqueous solution or H_2S and filling in H_2 gas or an aqueous solution, etc. [175–184]. Some studies have shown that hydrogen atoms are generated and penetrated through steel through electrochemical reactions, which may lead to degradation of structural integrity and cracking of microstructure defects [185, 186]. In addition, it was found that the interaction of hydrogen in steel is usually affected by the microstructure of the material [187]. According to the binding enthalpy with hydrogen, structural defects are divided into reversible traps (interstitial sites, dislocations and grain boundaries) and irreversible traps (precipitates, inclusions and voids) [188]. Hydrogen atoms remain permanently in irreversible traps but can escape reversible traps at room temperature [189]. Table 3 presents the values of trapping sites in iron and steel. It is seen that the trapping activation energies of hydrogen for defects like iron lattice, grain boundary, austenite/martensite interface, dislocation, austenite/dislocation boundary, micro-void and iron oxide interface are low, while those for ferrite/cementite interface and various nonmetallic inclusions such as chromium carbide, Y_2O_3, MnS, Al_2O_3, Fe_3C and a precipitate, TiC, are high.

Table 3 Trapping activation energies for various trapping sites in iron and steel [190]

Trapping site	Trapping activation energy ($kJ{\cdot}mol^{-1}$)	References
Reversible trapping site		
Iron lattice	5.4–7.1	[191]
Grain boundary	17.2–18.6	[192, 193]
Austenite/martensite interface	22	[194]
Dislocation	26.4–26.8	[192, 195]
Austenite/dislocation boundary	37	[194]
Microvoid	35.2–40	[192, 196]
Fe oxide interface	47	[171, 197]
Irreversible trapping site		
Ferrite/cementite interface	66.3–68.4	[170, 198]
Cr carbide interface	67	[199]
Y_2O_3 interface	70	[197]
MnS interface	72	[200, 201]
Al_2O_3 interface	79–86.2	[200, 202]
Fe_3C interface	84	[197]
TiC interface	68–137	[203, 204]

Some studies have focused on the effect of alloying elements on HE failure [205–207], indicating that the appropriate addition of Mn, Ti, Nb, V and Mo can optimize the microstructure and improve the resistance to HE. In the previous chapter, we know that the addition of W can improve the mechanical properties of alloy steel, and some scholars have studied the effect of the W addition on the HE resistance of alloy steel.

Zhao et al. [190] conducted a study on the effect of W additions (0, 0.1 wt.%, 0.5 wt.% and 1 wt.%) on the HE behavior of microalloyed steel. The total hydrogen desorbed by the heating process below 600 K was regarded as the diffusible hydrogen in the study. The effect of W on hydrogen desorption curves obtained after hydrogen charging of microalloyed steels with different W contents under the same conditions is shown in Fig. 20 [190]. The results show that the addition of W reduces the amount of diffused hydrogen in microalloyed steel.

Then the microstructures of microalloyed steel with different W content were observed, as shown in Fig. 21 [190]. The sample without W consists mainly of PF and pearlite accompanied by a small amount of AF, as shown in Fig. 21a. The addition of W significantly modifies the microstructure of the microalloyed steel. As presented in Fig. 21b, the amount of AF increases after adding 0.1 wt.% W compared to 0 wt.% W steel. As shown in Fig. 21c, the amount of AF surrounded by allotriomorphic ferrite increases significantly

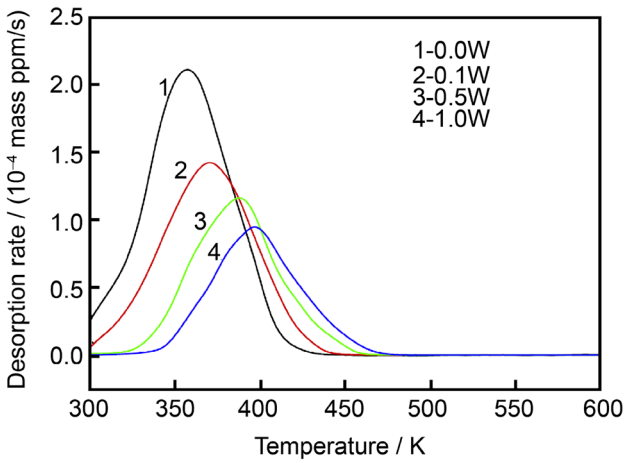

Fig. 20 Effects of W on the profile of hydrogen desorption curves under the hydrogen charging current density of 5 A·m^{-2} and heating rate of 100 K·h^{-1}. Reproduced with the permission from Ref. [190]. Copyright 2014 Elsevier

when the W content increases to 0.5 wt.%. When W increased from 0.5 wt.% to 1 wt.%, the allotriomorphic ferrite disappears and the microstructure transforms into a mixture of AF and bainite (Fig. 21d).

The permeability and diffusivity of hydrogen in the steel are in the order of PF and pearlite, AF and bainite [208]. In PF and pearlite, hydrogen permeability and diffusivity are the highest. This is attributed to the diffusion path along the ferrite/Fe_3C interface in dispersed fine-grain pearlite and the grain boundaries of ferrite since a large number of equiaxed grains refinement can form grain boundaries with large volume fractions, which can be available as a high diffusion path for hydrogen [209]. AF is characterized by short ferrite needles with a basket weave feature. This interlocking property and its fine grain size provide a larger grain boundary area as a hydrogen diffusion path and lead to a higher permeation rate. However, the randomly oriented needle-like ferrite interface affects the hydrogen transport and retards the hydrogen diffusion. In contrast, in bainite, the presence of Fe_3C becomes a barrier to hydrogen transport.

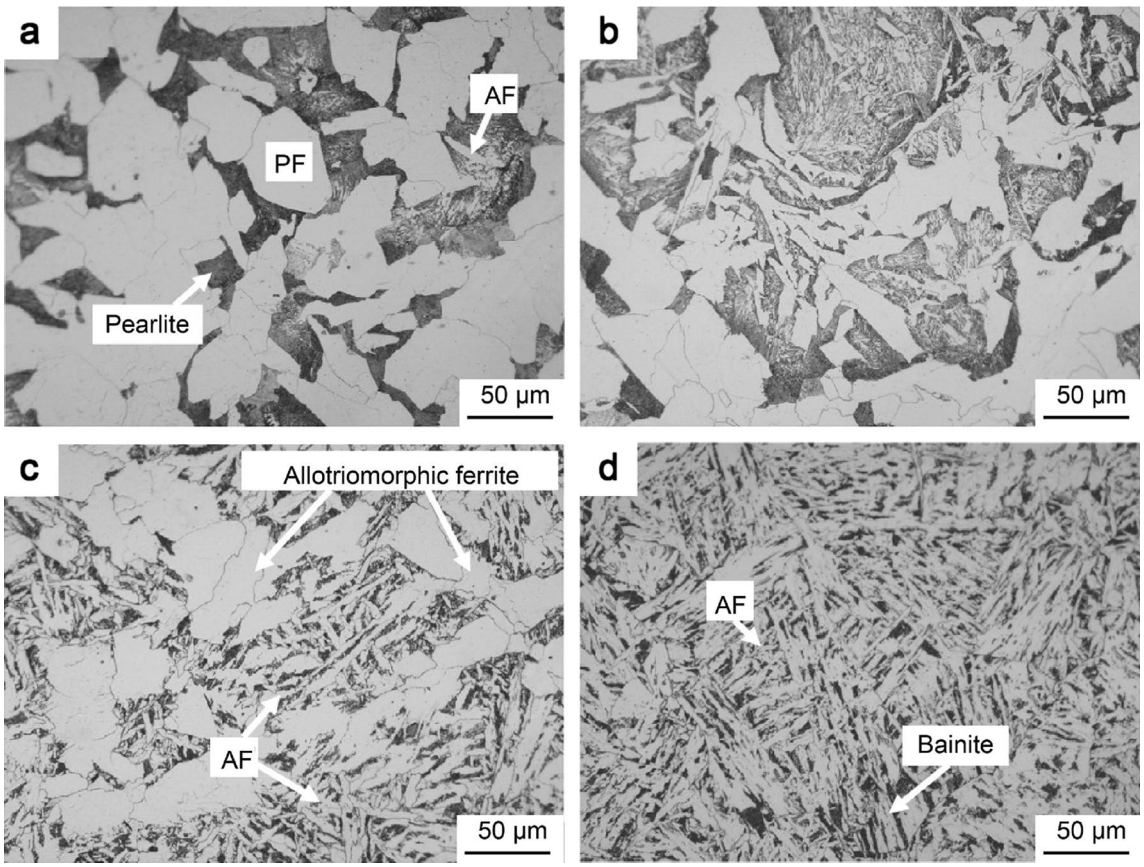

Fig. 21 Microstructures of the **a** 0 W, **b** 0.1 W, **c** 0.5 W and **d** 1 W steels. Reproduced with the permission from Ref. [190]. Copyright 2014 Elsevier

Table 4 Chemical composition of the Fe–C–W alloys in wt.% [210]

Material/element	C	W	Other
Alloy A	0.096	2.670	150–200 ppm Al
Alloy B	0.186	6.130	
Alloy C	0.277	8.700	

Therefore, hydrogen has the lowest permeability and diffusivity in bainite. It can be seen that the addition of W leads to a change in the microstructure of the microalloyed steel and further enhances the HE resistance of the alloy steel.

The effect of hydrogen on the mechanical properties of Fe–C–W alloys was studied by Depover et al. [210, 211]. The chemical composition is given in Table 4. It was found that the hydrogen trapping capacity increases with alloy A → B → C under tempering conditions at 500 °C and the hydrogen diffusion coefficient decreases with increasing carbon and W content. It is shown that W_2C induced by tempering above 20 nm cannot trap hydrogen. In contrast, the fine W_2C particles obtained by reducing the tempering time can trap more hydrogen, corresponding to an activation energy of 42–45 kJ·mol^{-1}. When tempered at 700 °C for 1 h, the trapped hydrogen content increases. This is related to the trapping ability of $W_{23}C_6$, which has a slightly higher activation energy between 47 and 49 kJ·mol^{-1}. This leads to increased resistance of alloy steel to hydrogen-induced mechanical degradation during tempering. Moreover, the addition of W inhibits the coarsening of the precipitated phase. The fine precipitated phase hinders the movement of dislocations and retards the transport of dislocation-trapped hydrogen to the crack-sensitive region, which improves the HE resistance of the alloy steel [212, 213].

In summary, the addition of W leads to changes in the microstructure of the alloy steel, which lowers the permeability and diffusivity of hydrogen. In addition, there are fine precipitation phases, such as W_2C and $W_{23}C_6$, which have a trapping effect on hydrogen. In turn, the resistance to HE of alloy steel is improved. Nonetheless, further research is needed on whether the higher W content of alloy steel can improve the resistance to HE.

7 Conclusions

Tungsten, as an alloying element, has been attracting increasing scientific and industrial attention due to its positive role in alloy steel. This paper has reviewed the effects of tungsten on the microstructure and properties of alloy steel, with the contents including the effects of tungsten on microstructure evolution, mechanical properties, hydrogen embrittlement and corrosion resistance. In the future, a lot of work can still be conducted to explore the optimal content of tungsten as an alloying element to enhance the properties of alloy steel and the technological conditions for producing tungsten-containing alloy steel without defects.

Due to the rapid pace of research in this field, it is impossible to check all the relevant studies being conducted in the world and some newly published articles may inevitably be missed. This paper has to the best of my knowledge presented a review of the effects of tungsten alloying on steel microstructure and properties in the hope that readers will gain inspiration from it.

Acknowledgements This research was supported by the Central Government Guided Local Science and Technology Development Fund Project (Grant No. YDZJSX2021A006), the Fund Program for the Scientific Activities of Selected Returned Overseas Professionals in Shanxi Province (Grant No. 20210035), and the Research Project Supported by Shanxi Scholarship Council of China (Grant No. 2020-037).

Declarations

Conflict of interest The authors declare no conflict of interest.

References

1. Yao G, Pan S, Yuan J, Guan Z, Li X. A novel process for manufacturing copper with size-controlled in-situ tungsten nanoparticles by casting. J Mater Process Technol. 2021;296:117187.
2. Han T, Hou C, Zhao Z, Huang X, Tang F, Li Y, Song X. W–Cu composites with excellent comprehensive properties. Compos B Eng. 2022;233:109664.
3. Higashino S, Miyake M, Ikenoue T, Hirato T. Formation of a photocatalytic WO_3 surface layer on electrodeposited Al–W alloy coatings by selective dissolution and heat treatment. Sci Rep. 2019;9(1):16008.
4. Zhao J, Jiang Z, Chong SL. Functions of tungsten alloying in microalloyed steels. New York: Nova Science Publishers; 2014.
5. Sohar CR. Lifetime controlling defects in tool steels. Berlin: Springer; 2011.
6. Davis JR. Heat-resistant materials. New York: ASM International; 1997.
7. Park JS, Kim SJ, Lee CS. Effect of W addition on the low cycle fatigue behavior of high Cr ferritic steels. Mater Sci Eng A. 2001;298(1–2):127.
8. Masuyama F. History of power plants and progress in heat resistant steels. ISIJ Int. 2001;41(6):612.
9. Irhzo A, Segui Y, Bui N, Dabosi F. The role of alloyed tungsten on the conductivity of stainless steel passive layers. Corros Sci. 1986;26(10):769.
10. Dou P, Kimura A, Kasada R, Okuda T, Inoue M, Ukai S, Ohnuki S, Fujisawa T, Abe F. Effects of titanium concentration and tungsten addition on the nano-mesoscopic structure of high-Cr oxide dispersion strengthened (ODS) ferritic steels. J Nucl Mater. 2013;442(1–3):S95.
11. Grzesik Z, Smola G, Adamaszek K, Jurasz Z, Mrowec S. High temperature corrosion of valve steels in combustion gases of petrol containing ethanol addition. Corros Sci. 2013;77:369.
12. Nam WJ, Lee CS, Ban DY. Improvement of sag resistance by the addition of tungsten in SiCrMoV steels. Scripta Mater. 1997;36(11):1315.

13. Jin IS, Chang NP, Hong SH, Kim YG. Development and properties of tungsten-bearing stainless maraging steels. Mater Sci Eng A. 1991;138(2):267.
14. Heo NH, Lee HC. Effect of tungsten addition on the ductile–brittle–ductile transition in Fe–8Mn–7Ni–W maraging steels. Scr Metall Mater. 1995;33(12):2031.
15. Yang HR, Lee KB, Kwon H. Effects of austenitizing treatments and inclusions on secondary hardening and fracture behavior for high Co–Ni steels containing W. Mater Sci Eng A. 1999;265(1–2):179.
16. Fernande CM, Rocha A, Cardoso JP, Bastos A. WC-stainless steel hardmetals. Int J Refract Metal Hard Mater. 2018;72:21.
17. Gu DD, Ma J, Chen HY, Lin KJ, Xi LX. Laser additive manufactured WC reinforced Fe-based composites with gradient reinforcement/matrix interface and enhanced performance. Compos Struct. 2018;192:387.
18. Heydari D, Skandani AA, Haik MA. Effect of carbon content on carbide morphology and mechanical properties of A.R. white cast iron with 10–12% tungsten. Mater Sci Eng A. 2012;542(Apr. 30):113.
19. Wurm FX. On tungsten steel. J Franklin Inst. 1860;70(1):42.
20. Fay H. The metallurgy of iron and steel. J Am Chem Soc. 1908;30(11):1793.
21. Neck CP, Bedeian AG, Frederick W, Taylor J. Maunsell White III, and the Matthew effect: the rest of the story. J Manag Hist. 1996;2(2):20.
22. Li J. Sand casting of metallic parts and structures. Encycl Mater Met Alloys. 2022;4:37.
23. Mehr FF, Cockcroft S, Reilly C, Maijer D. Investigation of the efficacy of a water-cooled chill on enhancing heat transfer at the casting-chill interface in a sand-cast A319 engine block. J Mater Process Technol. 2020;286:116789.
24. Kang JW, Ma QX. The role and impact of 3D printing technologies in casting. China Foundry. 2017;14:157.
25. Thomas PA, Aahlada PK, Kiran NS, Ivvala J. A review on transition in the manufacturing of mechanical components from conventional techniques to rapid casting using rapid prototyping. Mater Today Proc. 2018;5(5):11990.
26. Chen H, Ding TS, Li J, Xiao XS, Zhao JL, Jiang LZ. A new economical sigma-free duplex stainless steel 19Cr–6Mn–1.0Mo–0.5Ni–05W–0.5Cu–0.2N. J Iron Steel Res Int. 2011;18(4):52.
27. Tan Y, Ren S, Shi S, Wen S, Jiang D, Dong W, Ji M, Sun S. Removal of aluminum and calcium in multicrystalline silicon by vacuum induction melting and directional solidification. Vacuum. 2014;99:272.
28. Laha K, Saroja S, Moitra A, Sandhya R, Mathew MD, Jayakumar T, Rajendra KE. Development of India-specific RAFM steel through optimization of tungsten and tantalum contents for better combination of impact, tensile, low cycle fatigue and creep properties. J Nucl Mater. 2013;439(1–3):41.
29. Kim SB, Paik KW, Kim YG. Effect of Mo substitution by W on high temperature embrittlement characteristics in duplex stainless steels. Mater Sci Eng A. 1998;247(1–2):67.
30. Jeon SH, Kim ST, Lee IS, Kim JS, Kim KT, Park YS. Effects of W substitution on the precipitation of secondary phases and the associated pitting corrosion in hyper duplex stainless steels. J Alloys Compd. 2012;544:166.
31. Armaki HG, Maruyama K, Yoshizawa M, Igarashi M. Prevention of the overestimation of long-term creep rupture life by multiregion analysis in strength enhanced high Cr ferritic steels. Mater Sci Eng A. 2008;490(1–2):66.
32. Toda Y, Nakamura Y, Harada N, Kaseya A, Kobata N, Mitarai YY, Umezawa O. Effect of the Laves phase and carbide on the creep strength of Fe–C–15Cr–W alloys. Mater Sci Eng A. 2020;797:140104.
33. Fedoseeva A, Nikitin I, Dudova N, Kaibyshev R. Coarsening of Laves phase and creep behaviour of a Re-containing 10% Cr-3% Co-3% W steel. Mater Sci Eng A. 2021;812:141137.
34. Purba RH, Shimizu K, Kusumoto K, Todaka T, Shirai M, Hara H, Ito J. Erosive wear characteristics of high-chromium based multicomponent white cast irons. Tribol Int. 2021;159(24):106982.
35. Hosoi Y, Shimoide Y, Abraham M, Kutsuna M, Miyahara K. Influence of tungsten, carbon and nitrogen on toughness and weldability of low activation austenitic high manganese stainless steels. J Nucl Mater. 1992;191–194(Part B):686.
36. Klueh RL, Alexander DJ. Effect of vanadium and titanium on mechanical properties of chromium–tungsten steels. J Nucl Mater. 1994;212–215:569.
37. Nedjad SH, Garabagh MRM, Ahmadabadi MN, Shirazi H. Effect of further alloying on the microstructure and mechanical properties of an Fe–10Ni–5Mn maraging steel. Mater Sci Eng A. 2008;473(1–2):249.
38. Raj B, Rao KBS, Bhaduri AK. Progress in the development of reduced activation ferritic–martensitic steels and fabrication technologies in India. Fusion Eng Des. 2010;85(7–9):1460.
39. Mir HE, Jardy A, Bellot JP, Chapelle P, Lasalmonie D, Senevat J. Thermal behaviour of the consumable electrode in the vacuum arc remelting process. J Mater Process Technol. 2010;210(3):564.
40. Yang ZJ, Kou HC, Zhao XH, Li JS, Hu R, Chang H, Zhou L. Effect of remelting current on molten pool profile of titanium alloy ingot during vacuum arc remelting process. J Shanghai Jiaotong Univ (Sci). 2011;16:133.
41. Williamson RL, Beaman JJ, Melgaard DK. Optimal filtering applied to the vacuum arc remelting process. Materialsence. 2000;6:14.
42. Raju S, Ganesh BJ, Rai AK, Mythili R, Saroja S, Mohandas E, Vijayalakshmi M, Rao KBS, Raj B. Measurement of transformation temperatures and specific heat capacity of tungsten added reduced activation ferritic–martensitic steel. J Nucl Mater. 2009;389(3):385.
43. Kermanpur A, Lee PD, Mclean M, Tin S. Integrated modeling for the manufacture of aerospace discs: grain structure evolution. JOM. 2004;56(3):72.
44. Klueh RL, Alexander DJ, Kenik EA. Development of low-chromium, chromium–tungsten steels for fusion. J Nucl Mater. 1995;227(1–2):11.
45. Vanaja J, Laha K, Mathew MD, Jayakumar T, Kumar ER. Effects of tungsten and tantalum on creep deformation and rupture properties of reduced activation ferritic–martensitic steel. Proc Eng. 2013;55:271.
46. Fujikawa T, Manabe Y. Handbook of advanced ceramics. 2nd ed. Materials, applications, processing, and properties. 2013. p. 1203.
47. Grinder O. The HIP way to make cleaner, better steels. Met Powder Rep. 2007;62(9):16.
48. Eiselt CC, Klimenkov M, Lindau R, Möslang A. Characteristic results and prospects of the 13Cr–1W–0.3Ti–0.3Y2O3 ODS steel. J Nucl Mater. 2009;386–388:525.
49. Shinozuka K, Tamura M, Esaka H, Shiba K, Nakamura K. Creep behavior of oxide dispersion strengthened 8Cr–2WVTa and 8Cr–1W steels. J Nucl Mater. 2009;384(1):1.
50. Liu W, Zhang L, Ma Y, Cai Q, Zhu W, Wang R, Wen Z. Low temperature co-sintering of tungsten alloy/steel composite structure. Int J Refract Metal Hard Mater. 2020;90:105224.
51. Ninawe PS, Ganesh S, Karthik PS, Chandrasekhar SB, Vijay R. Microstructure and mechanical properties of spark plasma sintered austenitic ODS steel. Adv Powder Technol. 2022;33(6):103584.
52. Tan C, Wang GY, Ji L, Tong YG, Duan XM. Investigation on 316L/W functionally graded materials fabricated by mechanical alloying and spark plasma sintering. J Nucl Mater. 2016;469:32.

53. Zhang F, Reich M, Kessler O, Burkel E. The potential of rapid cooling spark plasma sintering for metallic materials. Mater Today. 2013;16(5):192.
54. Hu K, Li XQ, Yang C, Li YY. Densification and microstructure evolution during SPS consolidation process in W–Ni–Fe system. Trans Nonferrous Met Soc China. 2011;21(3):493.
55. Munir ZA, Tamburini UA, Ohyanagi M. The effect of electric field and pressure on the synthesis and consolidation of materials: a review of the spark plasma sintering method. J Mater Sci. 2006;41(3):763.
56. Madugundo R, Rao NVR, Schönhöbel AM, Salazar D, El-Gendy AA. Magnetic nanostructured materials. Micro Nano Technol. 2018;6:157.
57. Anselmi TU. Spark plasma sintering. Encycl Mater Tech Ceram Glasses. 2021;1:294.
58. Ordoñez MFC, Farias MCM, Machado IF, Souza RM. Effect of tungsten carbide addition on the tribological behavior of Astaloy 85Mo powder consolidated via spark plasma sintering. Tribol Int. 2018;127:313.
59. Koller M, Kruisova A, Musalek R, Matejicek J, Seiner H, Landa M. On the relation between microstructure and elastic constants of tungsten/steel composites fabricated by spark plasma sintering. Fusion Eng Des. 2018;133:51.
60. Matejicek J, Cech J, Nevrla B, Vilemova M, Hausild P, Klevarova V. Mechanical and thermal properties of individual phases formed in sintered tungsten–steel composites. Acta Phys Pol General Phys Phys Condens Matter Opt Quantum Electron Atom Mol Phys Appl Phys. 2015;128(4):718.
61. Nygren M, Shen Z. On the preparation of bio-, nano- and structural ceramics and composites by spark plasma sintering. Solid State Sci. 2003;5(1):125.
62. Sivakumar R, Guo S, Nishimura T, Kagawa Y. Thermal conductivity in multi-wall carbon nanotube/silica-based nanocomposites. Scripta Mater. 2007;56(4):265.
63. Watari F, Yokoyama A, Omori M, Hirai T, Kondo H, Uo M, Kawasaki T. Biocompatibility of materials and development to functionally graded implant for bio-medical application. Compos Sci Technol. 2004;64(6):893.
64. Zhang F, Shen J, Sun JF. The effect of phosphorus additions on densification, grain growth and properties of nanocrystalline WC–Co composites. J Alloys Compd. 2004;385(1):96.
65. Zhang F, Weidmann A, Nebe JB, Beck U, Burkel E. Preparation, microstructures, mechanical properties, and cytocompatibility of TiMn alloys for biomedical applications. J Biomed Mater Res B Appl Biomater. 2010;94B(2):406.
66. Gu YW, Khor KA, Cheang P. Bone-like apatite layer formation on hydroxyapatite prepared by spark plasma sintering (SPS). Biomaterials. 2004;25(18):4127.
67. Zhang F, Otterstein E, Burkel E. Spark plasma sintering, microstructures, and mechanical properties of macroporous titanium foams. Adv Eng Mater. 2010;12(9):863.
68. Zhang F, Sugar A, Jacobsen G, Collins M. Visual function and spectacle independence after cataract surgery: bilateral diffractive multifocal intraocular lenses versus monovision pseudophakia. J Cataract Refract Surg. 2011;37(5):853.
69. Mondal A, Agrawal D, Upadhyaya A. Microwave sintering of refractory metals/alloys: W, Mo, Re, W–Cu, W–Ni–Cu and W–Ni–Fe alloys. J Microw Power Electromagn Energy. 2010;44:28.
70. Yadoji P, Peelamedu R, Agrawal D, Roy R. Microwave sintering of Ni–Zn ferrites: comparison with conventional sintering. Mater Sci Eng B. 2003;98(3):269.
71. Oghbaei M, Mirzaee O. Microwave versus conventional sintering: a review of fundamentals, advantages and applications. J Alloys Compd. 2010;494(1–2):175.
72. Venkatesh VSS, Deoghare AB. Effect of microwave sintering on the mechanical characteristics of Al/kaoline/SiC hybrid composite fabricated through powder metallurgy techniques. Mater Chem Phys. 2022;287:126276.
73. Agrawal D. Microwave sintering of metal powders. Adv Powder Metall. 2013;361:1.
74. Jandyal A, Chaturvedi I, Wazir I, Raina A, Haq M. 3D printing—a review of processes, materials and applications in industry 4.0. Sustain Oper Comput. 2022;3:33.
75. Pan SH, Yao GC, Cui YN, Meng FS, Luo C, Zheng TQ, Singh G. Additive manufacturing of tungsten, tungsten-based alloys, and tungsten matrix composites. Tungsten. 2022;1:1.
76. Dorow-Gerspach D, Kirchner A, Loewenhoff T, Pintsuk G, Wirtz M. Additive manufacturing of high density pure tungsten by electron beam melting. Nucl Mater Energy. 2021;28(1–3):101046.
77. Yin X, Zhai Q, Zhang Q, Wang K, Wang L. Effect of tungsten particles on microstructure and properties of 316 L stainless steel manufactured by selective laser melting. J Manuf Process. 2021;68(3):210.
78. Ren X, Liu H, Lu F, Huang L, Yi X. Effects of processing parameters on the densification, microstructure and mechanical properties of pure tungsten fabricated by optimized selective laser melting: from single and multiple scan tracks to bulk parts. Int J Refract Metal Hard Mater. 2021;96:105490.
79. Bajaj P, Hariharan A, Kini A, Kürnsteiner P, Jägle EA. Steels in additive manufacturing: a review of their microstructure and properties. Mater Eng A. 2019;772:138633.
80. Kang N, Lu JL, Li QG, Cao YN, Mansori ME. A new way to net-shaped synthesis tungsten steel by selective laser melting and hot isostatic pressing. Vacuum. 2020;179:109557.
81. Clare AT, Mishra RS, Merklein M, Tan H, Bambach M. Alloy design and adaptation for additive manufacture. J Mater Process Technol. 2021;299:117358.
82. Kang N, Ma W, Heraud L, El Mansori M, Li F, Liu M, Liao H. Selective laser melting of tungsten carbide reinforced maraging steel composite. Addit Manuf. 2018;22:104.
83. Munir K, Biesiekierski A, Wen C, Li Y. Metallic biomaterials processing and medical device manufacturing. Woodh Publ Ser Biomater. 2020;235:1.
84. Yan ZA, Ld A, Fei LB, Kc C, Sw C. Effect of heat treatment on the microstructure and mechanical property of W/316 L multimaterial fabricated by selective laser melting. J Alloys Compd. 2022;890:161841.
85. Heuer S, Li BS, Armstrong DEJ, Zayachuk Y, Linsmeier C. Microstructural and micromechanical assessment of aged ultrafast sintered functionally graded iron/tungsten composites. Mater Des. 2020;191:108652.
86. Ganesh V, Leich L, Gerspach DD, Heuer S, Coenen JW, Wirtz M, Pintsuk G, Gormann F, Lied P, Baumgärtner S, Theisen W, Linsmeier C. Manufacturing of W/steel composites using electro-discharge sintering process. Nucl Mater Energy. 2022;30:101089.
87. Lee LHC. Effects of alloying elements on microstructure and fracture properties of cast high speed steel rolls: part I: microstructural analysis. Mater Sci Eng A. 1998;254(1):282.
88. Nascimento AMD, Ocelík V, Ierardi M, Hosson JTMD. Microstructure of reaction zone in WCp/duplex stainless steels matrix composites processing by laser melt injection. Surf Coat Technol. 2008;202(10):2113.
89. Matejicek J, Boldyryeva H, Brozek V, Sachr P, Chraska T, Pala Z. W-steel and W–WC-steel composites and FGMs produced by hot pressing. Fusion Eng Des. 2015;100:364.
90. Zhao J, Kim YW, Lee JH, Lee JM, Chang HS, Lee CS. Effect of tungsten addition on the mechanical properties and corrosion resistance of S355NL forging steel. Met Mater Int. 2012;18(2):217.

91. Zhao J, Jiang Z, Lee CS. Effects of tungsten addition and heat treatment conditions on microstructure and mechanical properties of microalloyed forging steels. Mater Sci Eng A. 2013;562:144.
92. Zhao J, Jiang Z, Ji SK, Chong SL. Effects of tungsten on continuous cooling transformation characteristics of microalloyed steels. Mater Des. 2013;49:252.
93. Froitzheim J, Meier G, Niewolak L, Ennis P, Hattendorf H, Singheiser L, Quadakkers WJ. Development of high strength ferritic steel for interconnect application in SOFCs. J Power Sources. 2008;178(1):163.
94. Korcakova L, Hald J, Somers MAJ. Quantification of Laves phase particle size in 9CrW steel. Mater Charact. 2001;47(2):111.
95. Smith CS. Precipitation hardening in the Fe–W system. J Appl Phys. 1941;12(11):817.
96. Jacob A, Schmetterer C, Singheiser L, Weale AG, Hallstedt B, Watson A. Modeling of Fe–W phase diagram using first principles and phonons calculations. Calphad. 2015;50:92.
97. Okamoto H. Supplemental literature review of binary phase diagrams: B–Fe, Cr–Zr, Fe–Np, Fe–W, Fe–Zn, Ge–Ni, La–Sn, La–Ti, La–Zr, Li–Sn, Mn–S, and Nb–Re. J Phase Equilib Diffus. 2016;37(5):1.
98. Henig ET, Hofman H, Petzow G. The constitution of W-Fe–Ni refractory metal alloys and the influence on the mechanical properties. Plansee Semin. 1981;335:1.
99. Zdziobek AA, Commeau T, Joubert JM. Partial redetermination of the Fe–W phase diagram. Metall Mater Trans A. 2013;44:2996.
100. Ichise E, Ueshima Y, Miyagawa S. Reexamination of the high temperature region of Fe–W binary alloy phase diagram. Tetsu-to-Hagane. 2009;72(7):791.
101. Kirchner G, Harvig H, Uhrenius B. Experimental and thermodynamic study of the equilibria between ferrite, austenite and intermediate phases in the Fe–Mo, Fe–W, and Fe–Mo–W systems. Metall Trans. 1973;4(4):1059.
102. Takemori T, Myeong Y, Wey TN. Effect of magnetic transition on the solubility of alloying elements in cobalt. J Jpn Inst Met. 1981;45(4):341.
103. Andersson JO, Gustafson P. A thermodynamic evaluation of the iron–tungsten system. Calphad Comput Coupling Phase Diagr Thermochem. 1983;7(4):317.
104. Kostakis G. Intermetallic phases of the system Fe–W. Z Metall Mater Res Adv Tech. 1985;76:34.
105. Gasik M. Handbook of ferroalloys. Theory and technology. New York: Butterworth-Heinemann; 2013. p. 37.
106. Uhrenius B. Calculation of phase equilibria in the Fe–W–C system. Calphad. 1980;4(3):173.
107. Gustafson P. A thermodynamic evaluation of the C–Fe–W system. Metall Mater Trans A. 1987;18(2):175.
108. Raghavan V. C–Fe–W (carbon–iron–tungsten). J Phase Equil. 1994;15:429.
109. Tang D, Liu X, Xiao W. Influences of W contents on microstructures, mechanical properties and the shielding performance for neutrons and γ-rays of Fe–W–C alloy. J Alloys Compd. 2020;827:153932.
110. Eryomina MA, Lomayeva SF, Lyalina NV, Syugaev AV, Tarasov VV. Structure and properties of mechanosynthesized W–Fe–C carbides. Mater Today Proc. 2020;25:356.
111. Eryomina MA, Lomayeva SF, Kharanzhevsky EV, Tarasov VV, Dementyev VB. Phase composition and wear resistance of compacts and coatings based on carbides fabricated in W–Fe–C system by wet mechanical alloying. Proc Struct Integr. 2021;32:284.
112. Gustafson P. An experimental study and a thermodynamic evaluation of the Cr–Fe–W system. Metall Mater Trans A. 1988;19(10):2531.
113. Larry K, Harvey N. Calculation of superalloy phase diagrams: part IV. Metall Mater Trans A. 1975;6(11):2115.
114. Yin YF, Faulkner RG. Modelling the effects of alloying elements on precipitation in ferritic steels. Mater Sci Eng A. 2003;344(1–2):92.
115. Liu Z, Liu Z, Wang X, Chen Z, Ma L. Evolution of the microstructure in aged G115 steels with the different concentration of tungsten. Mater Sci Eng A. 2018;729:161.
116. Niewola L, Zurek J, Wessel E, Hattendorf H, Quadakkers WJ. Temperature dependence of phase composition in W and Si-alloyed high chromium ferritic steels for SOFC interconnect applications. J Alloys Compd. 2017;717:240.
117. Yun DW, Seo HS, Jun JH, Lee JM, Kim DH, Kim KY. Oxide modification by chi phase formed on oxide/metal interface of Fe–22Cr–0.5Mn ferritic stainless steel for SOFC interconnect. Int J Hydrog Energy. 2011;36(9):5595.
118. Ahmad J, Asami K, Takeuchi A, Louzguine DV, Inoue A. High strength Ni–Fe–W and Ni–Fe–W–P alloys produced by electrodeposition. Mater Trans. 2003;44(10):1942.
119. Korniyenko K. Iron–oxygen–tungsten. Ternary Alloy Syst. 2009;11D5:453.
120. Guillermet AF. Thermodynamic calculation of the Fe–Co–W phase diagram. Int J Mater Res. 1988;79:633.
121. Yang JR, Bhadeshia HKDH. The dislocation density of acicular ferrite in steel welds. Welding Res Suppl. 1990;305:1.
122. Bhadeshia H. Bainite in steels. 2nd ed. Cambridge: The University Press; 2001. p. 26.
123. Graf MK, Hillenbrand HG, Peters PA, in: PD Southwick (Ed.). Accelerated cooling of steel. TMS-AIME, New York. 1985. 349.
124. Jung S, Jeon C, Yong HJ, Choi WM, Lee BJ, Oh YJ, Jang S, Lee S. Effects of tungsten and molybdenum on high-temperature tensile properties of five heat-resistant austenitic stainless steels. Mater Sci Eng A. 2016;656:190.
125. Salama E, Eissa MM, Tageldin AS. Distinct properties of tungsten austenitic stainless alloy as a potential nuclear engineering material. Nucl Eng Technol. 2019;51(3):784.
126. Zhu H, He HF, Wang C, Zhang J, Zhu XH. Decomposition laws of tungsten prices fluctuation since 1900 and its applications. Trans Nonferrous Met Soc China. 2013;23(9):2807.
127. Chen H, Ye L, Han Y, Chen C, Fan J. Additive manufacturing of W–Fe composites using laser metal deposition: microstructure, phase transformation, and mechanical properties. Mater Sci Eng A. 2021;811:141036.
128. Wang D, Wang Z, Li K, Ma J, Liu W, Shen Z. Cracking in laser additively manufactured W: initiation mechanism and a suppression approach by alloying. Mater Des. 2019;162:384.
129. Huang L, An Q, Geng L, Wang S, Jiang S, Cui X, Zhang R, Sun F, Jiao Y, Chen X. Titanium matrix composites: multiscale architecture and superior high-temperature performance of discontinuously reinforced titanium matrix composite. Adv Mater. 2021;33(6):2170039.
130. Liu L, Ding Q, Yuan Z, Ji Z, Shen Z. Dislocation network in additive manufactured steel breaks strength-ductility trade-off. Mater Today. 2017;21(4):354.
131. Liu A, Wang L, Pan L, Cheng X. Microstructure and mechanical properties of a novel high-density steel having high tungsten content. Mater Sci Eng A. 2021;824:141797.
132. Ren X, Wang R, Wei D, Huang Y. Effect of scanning electron beam surface tungsten alloying on microstructure and hardness. Mater Lett. 2021;308:131190.
133. Wang B, Fu W, Yong L, Ping J, Zhang W, Tian Y. Study of the phase diagram and continuous cooling transformation of 12%Cr ultra-super-critical rotor steel. Mater Charact. 2008;59(8):1133.

134. Zhang Y, Sun Y, Guan S, Deng X, Yan X. Effect of titanium and tungsten on the structure and properties of heat-abrasion resistant steel. Mater Sci Eng A. 2008;478(1–2):214.
135. Yan JB, Gao YM, Fang Y, Yao C, Ye Z, Yi D, Ma S. Effect of tungsten on the microstructure evolution and mechanical properties of yttrium modified HP40Nb alloy. Mater Sci Eng A. 2011;529:361.
136. Srivastava AK, Das K. Microstructural and mechanical characterization of in situ TiC and (Ti, W)C-reinforced high manganese austenitic steel matrix composites. Mater Sci Eng A. 2009;516(1–2):1.
137. Chen X, Zhao L, Li D, Jiang L, Wang H. Characteristics of microwave melting H13 steel powder with different tungsten contents. Mater Lett. 2021;294(12):129803.
138. Lv Y, Sun Y, Zhao J, Yu G, Shen J, Hu S. Effect of tungsten on microstructure and properties of high chromium cast iron. Mater Des. 2012;39:303.
139. Mousavi ASH, Bahrami A, Varahram N, Davami P. Effects of tungsten on erosion-corrosion behavior of high chromium white cast iron. Mater Sci Eng A. 2007;454–455:623.
140. Klueh RL, Maziasz PJ, Alexander DJ. Bainitic chromium–tungsten steels with 3 Pct chromium. Metall and Mater Trans A. 1997;28(2):335.
141. Pickering FB. Transformation and hardenability in steels. Ann Arbor: Climax Molybdenum Co.; 1967. p. 109.
142. Zhang ZX, Ran QX, Xu YL, Yu XJ, Jiang DW, Xiao XS. A new series of Mo-free 21.5Cr–3.5Ni–xW–0.2N economical duplex stainless steels. J Iron Steel Res Int. 2014;21(1):69.
143. Sakasegawa H, Hirose T, Kohyama A, Katoh Y, Harada T, Asakura K, Kumagai T. Effects of precipitation morphology on toughness of reduced activation ferritic/martensitic steels. J Nucl Mater. 2002;307–311:490.
144. Miyahara K, Kobayashi Y, Hosoi Y. Effects of W and Mn on the mechanical properties, microstructure and aging behaviors of 10% Cr ferritic steels considered as reduced radio-activation materials. J Nucl Mater. 1991;179(Part-P1):667.
145. Abe F, Noda T, Araki H, Nakazawa S. Alloy composition selection for improving strength and toughness of reduced activation 9Cr–W steels. J Nucl Mater. 1991;179(Part-P1):663.
146. Abe F, Noda T, Okada M. Optimum alloy compositions in reduced-activation martensitic 9Cr steels for fusion reactor. J Nucl Mater. 1992;195(1–2):51.
147. Jang MH, Moon J, Kang JY, Ha HY, Lee C. Effect of tungsten addition on high-temperature properties and microstructure of alumina-forming austenitic heat-resistant steels. Mater Sci Eng A. 2015;647:163.
148. Abe F. Creep rates and strengthening mechanisms in tungsten-strengthened 9Cr steels. Mater Sci Eng A. 2001;319–321:770.
149. Li Q. Precipitation of Fe2W laves phase and modeling of its direct influence on the strength of a 12Cr–2W steel. Metall Mater Trans A. 2006;37(1):89.
150. Abe F, Nakazawa S, Araki H, Noda T. The role of microstructural instability on creep behavior of a martensitic 9Cr–2W steel. Metall Trans A. 1992;23(2):469.
151. Mediratta SR, Ramaswamy V, Singh V, Rao PR. Low cycle fatigue of dual phase steels produced by different cooling rates and a ferrite-pearlite steel. Scr Metall Mater. 1990;24(4):793.
152. Shankar V, Mariappan K, Nagesha A, Reddy GVP, Sandhya R, Mathew MD, Jayakumar T. Effect of tungsten and tantalum on the low cycle fatigue behavior of reduced activation ferritic/martensitic steels. Fusion Eng Des. 2012;87(4):318.
153. Abe F. Coarsening behavior of lath and its effect on creep rates in tempered martensitic 9Cr–W steels. Mater Sci Eng A. 2004;387(Dec):565.
154. Schmuki P. From Bacon to barriers: a review on the passivity of metals and alloys. J Solid State Electrochem. 2002;6(3):145.
155. Galvele JR, Lumsden JB, Staehle RW. Effect of molybdenum on the pitting potential of high purity 18% Cr ferritic stainless steels. J Electrochem Soc. 1978;125(8):1204–8.
156. Jargelius P. Electrochemical investigation of the influence of nitrogen alloying on pitting corrosion of austenitic stainless steels. Corros Sci. 1999;41(8):1639–64.
157. Goetz R, Laurent J, Landolt D. The influence of minor alloying elements on the passivation behaviour of iron-chromium alloys in HCl. Corros Sci. 1985;25(12):1115–26.
158. Tomio A, Sagara M, Doi T, Amaya H, Otsuka N, Kudo T. Role of alloyed copper on corrosion resistance of austenitic stainless steel in H2S-Cl-environment. Corros Sci. 2014;81:144–51.
159. Malik AU, Siddiqi NA, Ahmad S, Andijani IN. The effect of dominant alloy additions on the corrosion behavior of some conventional and high alloy stainless steels in seawater. Corros Sci. 1995;37:1521.
160. Herbsleb G. Influence of SO2, H2S and CO on pitting corrosion of austenitic chromium-nickel stainless steels with up to 4 wt% molybdenum in 1 M NaCl. Werkstoffe Korros. 1982;33:334.
161. Merello R, Botana FJ, Botella J, Matres MV, Marcos M. Influence of chemical composition on the pitting corrosion resistance of non-standard low-Ni high-Mn-N duplex stainless steels. Corros Sci. 2003;45(5):909.
162. Sedriks AJ. Corrosion of stainless steels. 2nd ed. New York: Wiley; 1996.
163. Bui N, Irhzo A, Dabosi F, Maire YL. On the mechanism for improved passivation by additions of tungsten to austenitic stainless steels. Passivity Met Semicond. 1983;39(12):599.
164. Davison RM, Laurin TR, Redmond JD, Watanabe H, Semchyshen M. A review of worldwide developments in stainless steels. Mater Des. 1986;7(3):111.
165. Lo KH, Shek CH, Lai JKL. Recent developments in stainless steels. Mater Sci Eng R Rep. 2009;65(4–6):39.
166. Ahn MK, Kwon HS, Lee HM. Quantitative comparison of the influences of tungsten and molybdenum on the passivity of Fe–29Cr ferritic stainless steels. Corros Sci. 1998;40(2):307.
167. Park CJ, Kwon HS. Effects of aging at 475 °C on corrosion properties of tungsten-containing duplex stainless steels. Corros Sci. 2002;44(12):2817.
168. Torres C, Hazarabedian MS, Quadir Z, Johnsen R, Iannuzzi M. The role of tungsten on the phase transformation kinetics and its correlation with the localized corrosion resistance of 25Cr super duplex stainless steels. J Electrochem Soc. 2020;167(8):081510.
169. Li J, Ye D, Chen YM, Su J, Zhao KY. Effect of chloric ions and temperature on the pitting corrosion behavior of supermartensitic stainless steel in CO_2-saturated chloride solution. Adv Mater Res. 2012;538–541:2342.
170. Wang M, Akiyama E, Tsuzaki K. Effect of hydrogen on the fracture behavior of high strength steel during slow strain rate test. Corros Sci. 2007;49(11):4081.
171. Michler T, Balogh MP. Hydrogen environment embrittlement of an ODS RAF steel—role of irreversible hydrogen trap sites. Int J Hydrog Energy. 2010;35(18):9746.
172. Escobar DP, Depover T, Wallaert E, Duprez L, Verhaege M, Verbeken K. Thermal desorption spectroscopy study of the interaction between hydrogen and different microstructural constituents in lab cast Fe–C alloys. Corros Sci. 2012;65:199.
173. Michler T, Naumann J. Microstructural aspects upon hydrogen environment embrittlement of various bcc steels. Int J Hydrogen Energy. 2010;35(2):821.
174. Esaklul KA. Trends in oil and gas corrosion research and technologies. Woodh Publ Ser Energy. 2017;315:1.
175. Slifka AJ, Drexler ES, Nanninga N, Levy Y, McColskey JD, Amaro RL. Fatigue crack growth of two pipeline steels in a pressurized hydrogen environment. Corros Sci J Environ Degrad Mater Control. 2014;78:313.

176. Wang G, Yan Y, Li J, Huang J, Su Y, Qiao L. Hydrogen embrittlement assessment of ultra-high strength steel 30CrMnSiNi2. Corros Sci. 2013;77:273.
177. Javidi M, Horeh SB. Investigating the mechanism of stress corrosion cracking in near-neutral and high pH environments for API 5L X52 steel. Corros Sci. 2014;80:213.
178. Koyama M, Akiyama E, Sawaguchi T, Ogawa K, Tsuzakia K. Hydrogen-assisted quasi-cleavage fracture in a single crystalline type 316 austenitic stainless steel. Corros Sci. 2013;75(7):345.
179. Qian L, Irwanto B, Atrens A. The influence of hydrogen on 3.5NiCrMoV steel studied using the linearly increasing stress test. Corros Sci. 2013;67:193.
180. Zheng S, Qi Y, Chen C, Li S. Effect of hydrogen and inclusions on the tensile properties and fracture behaviour of A350LF2 steels after exposure to wet H2S environments. Corros Sci. 2012;60:59.
181. Jackson HF, Nibur KA, Marchi CS, Puskar JD, Somerday BP. Hydrogen-assisted crack propagation in 304L/308L and 21Cr–6Ni–9Mn/308L austenitic stainless steel fusion welds. Corros Sci. 2012;60:136.
182. Koyama M, Akiyama E, Tsuzaki K. Effect of hydrogen content on the embrittlement in a Fe–Mn–C twinning-induced plasticity steel. Corros Sci. 2012;59:277.
183. Mustapha A, Charles EA, Hardie D. Evaluation of environment-assisted cracking susceptibility of a grade X100 pipeline steel. Corros Sci. 2012;54:5.
184. Koyama M, Akiyama E, Tsuzaki K. Hydrogen embrittlement in a Fe–Mn–C ternary twinning-induced plasticity steel. Corros Sci. 2012;54:1.
185. Kawashima A, Hashimoto K, Shimodaira S. Hydrogen electrode reaction and hydrogen embrittlement of mild steel in hydrogen sulfide solutions. Corrosion. 2013;32(8):321.
186. Novak P, Yuan R, Somerday BP, Sofronis P, Ritchie RO. A statistical, physical-based, micro-mechanical model of hydrogen-induced intergranular fracture in steel. J Mech Phys Solids. 2010;58(2):206.
187. Frappart S, Feaugas X, Creus J, Thebault F, Delattre L, Marchebois H. Study of the hydrogen diffusion and segregation into Fe–C–Mo martensitic HSLA steel using electrochemical permeation test. J Phys Chem Solids. 2010;71(10):1467.
188. Hirth JP. Effects of hydrogen on the properties of iron and steel. Metall Trans A. 1980;11(6):861.
189. Takai K, Watanuki R. Hydrogen in trapping states innocuous to environmental degradation of high-strength steels. ISIJ Int. 2003;43(4):520.
190. Zhao J, Jiang Z, Lee CS. Effects of tungsten on the hydrogen embrittlement behaviour of microalloyed steels. Corros Sci. 2014;82:380.
191. Kiuchi K, Mclellan RB. The solubility and diffusivity of hydrogen in well-annealed and deformed iron. Acta Metall. 1983;31(7):961.
192. Choo WY, Lee JY. Thermal analysis of trapped hydrogen in pure iron. Metall Trans A. 1982;13(1):135.
193. Kang HJ, Yoo JS, Ji TP, Ahn ST, Kang N, Cho KM. Effect of nano-carbide formation on hydrogen-delayed fracture for quenching and tempering steels during high-frequency induction heat treatment. Mater Sci Eng A. 2012;543:6.
194. Chun YS, Kim JS, Park KT, Lee YK, Lee CS. Role of ε martensite in tensile properties and hydrogen degradation of high-Mn steels. Mater Sci Eng A. 2012;533:87.
195. Lee JY, Lee JL. A trapping theory of hydrogen in pure iron. Philos Mag A. 1987;56(3):293.
196. Lee JL, Lee JY. Identification of defects generated during cathodic charging in pure iron by thermal analysis technique. Metall Trans A. 1985;16(3):468.
197. Maroef I, Olson DL, Eberhart M, Edwards GR. Hydrogen trapping in ferritic steel weld metal. Metall Rev. 2002;47(4):191.
198. Ji SK, You HL, Lee DL, Park KT, Chong SL. Microstructural influences on hydrogen delayed fracture of high strength steels. Mater Sci Eng A. 2009;505(3):105.
199. Oriani RA, Hirth JP, Smialowski M. Hydrogen degradation of ferrous alloys. New York: Noyes Publications; 1985.
200. Lee KY, Lee JY, Kim DR. A study of hydrogen-trapping phenomena in AISI 5160 spring steel. Mater Sci Eng. 1984;67(2):213.
201. Lee JL, Lee JY. Hydrogen trapping in AISI 4340 steel. Met Sci. 1983;17(9):426.
202. Lee JL, Lee JY. The interaction of hydrogen with Al_2O_3 particles in iron. Metall Trans A. 1986;17(12):2183.
203. Wei FG, Tsuzaki K. Quantitative analysis on hydrogen trapping of TiC particles in steel. Metall Mater Trans A. 2006;37(2):331.
204. Pressouyre GM, Bernstein IM. A quantitative analysis of hydrogen trapping. Metall Trans A. 1978;9:1571.
205. Hejazi D, Haq AJ, Yazdipour N, Dunne DP, Calka A, Barbaro F, Pereloma EV. Effect of manganese content and microstructure on the susceptibility of X70 pipeline steel to hydrogen cracking. Mater Sci Eng A. 2012;551:40.
206. Haq AJ, Muzaka K, Dunne DP, Calka A, Pereloma EV. Effect of microstructure and composition on hydrogen permeation in X70 pipeline steels. Int J Hydrogen Energy. 2013;38(5):2544.
207. Liao CM, Lee JL. Effect of molybdenum on sulfide stress cracking resistance of low-alloy steels. Corrosion. 2012;50(9):695.
208. Wang SH, Luu WC, Ho KF, Wu JK. Hydrogen permeation in a submerged arc weldment of TMCP steel. Mater Chem Phys. 2003;77(2):447.
209. Luu WC, Wu JK. The influence of microstructure on hydrogen transport in carbon steels. Corros Sci. 1996;38(2):239.
210. Depover T, Verbeken K. Thermal desorption spectroscopy study of the hydrogen trapping ability of W based precipitates in a Q&T matrix. Int J Hydrogen Energy. 2018;43(11):5760.
211. Depover T, Wallaert E, Verbeken K. On the synergy of diffusible hydrogen content and hydrogen diffusivity in the mechanical degradation of laboratory cast Fe–C alloys. Mater Sci Eng A. 2016;664:195.
212. Zhao MC, Ming L, Atrens A, Shan YY, Ke Y. Effect of applied stress and microstructure on sulfide stress cracking resistance of pipeline steels subject to hydrogen sulfide. Mater Sci Eng A. 2008;478(1–2):43.
213. Wang XT, Liu M, Zhou GY, Jiang H, Li X, Luo M, Liu YH, Zhang ZH, Cao GH. Effects of chromium and tungsten on sulfide stress cracking in high strength low alloy 125 ksi grade casing steel. Corros Sci. 2019;160:108163.